

# 中国激光

## 激光选区熔化成形 316L 不锈钢工艺、微观组织、力学性能的研究现状

蒋华臻<sup>1</sup>, 房佳汇钰<sup>1,2</sup>, 陈启生<sup>1,2\*</sup>, 姚少科<sup>1,2</sup>, 孙辉磊<sup>3</sup>, 侯静宇<sup>1,2</sup>, 胡琦芸<sup>1,2</sup>, 李正阳<sup>1,2\*\*</sup>

<sup>1</sup>中国科学院力学研究所宽域飞行工程科学与应用中心, 北京 100190;

<sup>2</sup>中国科学院大学工程科学学院, 北京 100049;

<sup>3</sup>河北科技大学机械工程学院, 河北 石家庄 050018

**摘要** 增材制造涉及快速的非平衡热过程, 导致成形件中存在大量的亚稳相和缺陷, 这些亚稳相和缺陷在构件服役过程中极易成为失效源。因此, 打印态构件一般都要经过热处理才能充分发挥其潜在的性能优势。近年来, 国内外许多研究机构在激光选区熔化(SLM)制备 316L 不锈钢方面取得了突破, SLM-316L 不锈钢打印态的强度和韧性都远远超过锻件, 这是因为材料内部形成了跨越 6 个数量级的非均匀层级结构(包括晶粒、缺陷、熔池、胞结构、纳米氧化物颗粒), 这是增材制造通过其特殊的非平衡热过程调控材料微结构的结果。316L 不锈钢具有面心立方结构, 在冷却至室温过程中不发生固态相变, 这种特性非常有利于开展基础研究, 揭示增材制造材料跨尺度结构对其性能的影响规律。本文详细阐述了 SLM-316L 不锈钢成形在工艺、跨尺度结构及力学性能方面的研究现状, 结合笔者的工作, 阐明并分析了 SLM-316L 不锈钢具有高强高韧力学性能的主流学术观点, 展望了该材料今后的重点研究方向。

**关键词** 激光技术; 增材制造; 激光选区熔化; 316L 不锈钢; 非均匀层级结构; 力学性能

中图分类号 TH164

文献标志码 A

DOI: 10.3788/CJL202249.1402804

### 1 引 言

金属增材制造(MAM)是一种用于生产复杂金属零件的新兴技术, 与传统材料合成及制备工艺相比, 它的最大优势在于能够在较短的交货周期内生产复杂或定制化的零件, 已在个性化生物植入体<sup>[1]</sup>、大型复杂航空发动机叶盘<sup>[2]</sup>、热核反应堆真空容器<sup>[3]</sup>等制造领域得到了广泛应用。随着粉末材料冶金制备技术、高质量低成本激光器、在线监测技术及相关软硬件的协同发展, 增材制造技术在工艺开发、材料微结构及力学性能等方面的研究都取得了重要进展<sup>[4]</sup>。美国材料与试验协会(ASTM Standard F2792-12a<sup>[5]</sup>)将增材制造的学术名词统一为定向能量沉积(DED)和粉末床熔化(PBF), 其中, 以激光为热源的 DED 与 PBF 成形是上述两类增材制造方式应用的最典型代表, 它们分别被称为激光金属沉积(LMD)和激光选区熔化(SLM)。这两种制造方法的共同之处是利用高能束热流将材料快速熔化形成熔池, 接着熔池以极高的冷却速率凝固。其差异性在于: LMD 的成形效率较高, 理论上无成形尺寸的限制,

对于大型复杂构件的制造具有独特优势, 其缺点是成形精度较低; SLM 因具有较高的空间分辨率(一般为几十微米), 能够制造精度较高的零部件, 其缺点是成形尺寸受舱室体积的限制, 且成形效率相对较低。

近年来, SLM 材料在制备工艺、微观组织和力学性能方面的研究性论文及综述性论文呈大幅增长的趋势<sup>[4,6-12]</sup>。SLM 是一项相对较新且快速发展的先进制造技术, 对其发展进行定期的批判性评估是必要的。316L 属于低碳奥氏体不锈钢, 其可焊性强, 且具有优异的耐蚀性和抗氧化性, 是一种用途广泛的结构材料。该钢在从熔融态冷却至室温过程中通常不发生固态相变<sup>[13-15]</sup>, 物理冶金过程相对简单, 是进行增材制造的首选材料。大量的研究已表明 SLM-316L 技术优于传统制造工艺, 但 SLM 过程由于涉及粉末逐层熔化与凝固带来的循环热作用, 在打印态材料中会不可避免地存在一些独特的微观组织特征, 如熔池<sup>[16]</sup>、缺陷<sup>[17]</sup>、沿打印方向生长的柱状晶<sup>[18]</sup>、胞结构<sup>[19]</sup>、残余应力<sup>[20]</sup>、纳米氧化物颗粒<sup>[21]</sup>, 这些复杂的微观结构的影响因素多达 130 多个<sup>[22]</sup>。

收稿日期: 2021-12-13; 修回日期: 2022-01-04; 录用日期: 2022-02-11

基金项目: 国家自然科学基金(11772344)

通信作者: \*qschen@imech.ac.cn; \*\*zyli@imech.ac.cn

为了解 SLM-316L 材料在复杂热循环作用下的微观组织及力学性能演化规律, 科研工作者进行了大量的研究工作, 建立起了 SLM 工艺参数与微观组织、力学性能之间的关系<sup>[19,23-26]</sup>, 这对于推动 SLM 技术的工业应用以及揭示该技术下的关键基础科学问题起到了积极作用。然而, 与传统的铸造、锻造等生产工艺相比, SLM-316L 材料由于复杂的冶金因素导致成形件内部形成跨越 6 个数量级的微观结构<sup>[19,24]</sup>, 因而材料的组织和性能更难以控制, 这也给理解 SLM-316L 成形过程所涉及的基础科学问题提出了重大挑战。

本文以研究较为广泛但综述论文却较少的 316L 不锈钢为对象<sup>[27]</sup>, 以其形成的跨尺度层级结构为基本论述点, 综述了打印态 SLM-316L 在致密度、熔池、晶粒、胞结构、位错密度及原位形成的纳米氧化物颗粒等方面的研究现状, 总结了 SLM-316L 材料在硬度、拉伸力学性能和耐蚀性等方面的研究进展, 同时对热处理后 SLM-316L 不锈钢微结构及力学性能的演化规律进行了简要概括。笔者认为, SLM-316L 不锈钢的非均匀层级结构在拉伸变形过程中作为一个整体对载荷的传递和应变的分配产生影响, 进而对材料的力学性能产生影响, 因此, 本文给出了 SLM-316L 层级结构中熔池、晶粒及胞结构在不同应变状态下的演化规律。特别地, 本文对 SLM-316L 获得高致密度零件的工艺参数(几种能量密度指标)控制、胞结构的形成机理以及打印态 SLM-316L 强韧兼备的机理进行了重点论述。

## 2 SLM 关键工艺参数及其对致密度的影响

### 2.1 SLM 缺陷的产生机理

SLM 涉及非平衡快速熔化、凝固的复杂冶金过程, 它涉及的物理现象包括激光与粉末的相互作用、粉末颗粒与成形舱室环境的对流/热交换、粉末颗粒之间的热传导、材料熔化后元素的再分配、元素之间的化学反应及凝固过程中微观组织的演变等。该成形过程不可避免地会在零件内部形成各种缺陷, 图 1 总结了 SLM 成形过程中形成的几种典型缺陷<sup>[4,17,28]</sup>, 包括特征尺寸较小的孔洞缺陷、特征尺寸较大的未熔合缺陷、凝固过程中出现的长条状裂纹缺陷以及低熔点元素蒸发造成的元素损失等。这些缺陷形成的机理是不同的: 孔洞的形成主要与粉末的铺粉密度、制粉工艺及粉末本身的特征有关<sup>[17]</sup>; 未熔合缺陷主要是由输入到粉末床的能量不足导致的<sup>[29]</sup>; 裂纹缺陷的产生主要是因为熔池内部较高的温度梯度和凝固速率导致成形件的内应力较大, 它与材料的热物性参数有关, 热传导系数较低而热膨胀系数较大的材料, 譬如不锈钢、镍基高温合金等, 易形成裂纹缺陷<sup>[17]</sup>; 元素损失主要是由于熔池局部区域的温度超过了某些合金元素的沸点, 而且有研究发现, 不同工艺参数导致的熔池形状及其温度分布决定了元素是否发生蒸发<sup>[30]</sup>。总之, 不论成形件中出现何种缺陷, 都主要是由工艺参数的不当组合导致的, 因此, 确定合适的成形工艺窗口是成形近乎完全致密零件的基础。

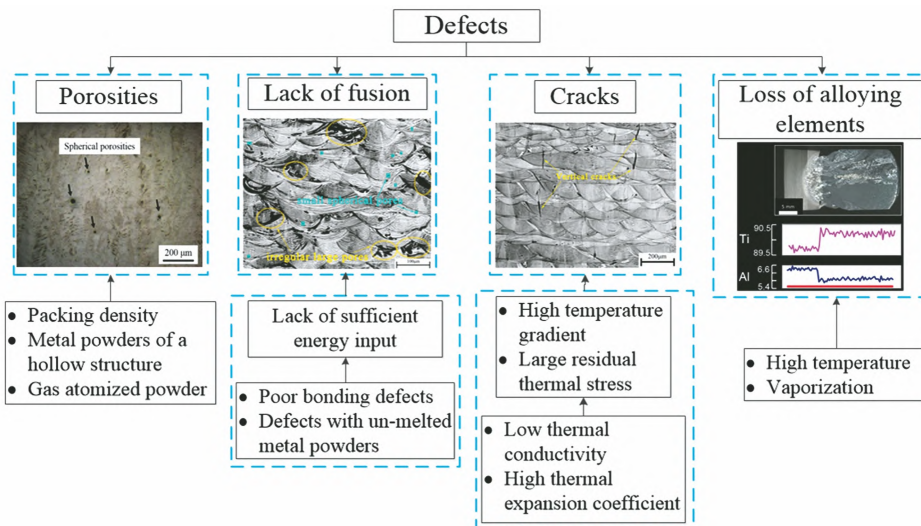


图 1 SLM 的几种典型缺陷形式(图中的照片摘自文献[4,17,28])

Fig. 1 Summary of defect types during selective laser melting process (the inset figures are collected from references[4,17,28])

### 2.2 常用的几个度量指标

高能密度的热源输入粉末床后, 粉末会在极短的时间(一般为  $10^{-4} \sim 10^{-5} \text{ s}$ <sup>[31]</sup>)内熔化形成熔池。除了粉末质量(如流动性、封装密度、尺寸、形状及分布等)<sup>[32]</sup>、扫描策略<sup>[33]</sup>外, 一般认为 SLM 中最为重要的工艺参数是激光功率、扫描速度、搭接间距、层厚、光斑

直径, 这些参数均会影响成形件内部缺陷的数量及形貌, 进而对最终样件的力学性能产生影响<sup>[23,34-35]</sup>。不同的粉末材料体系由于热物性参数的差异会形成不同的温度场或具有不同的凝固动力学特征, 因而会产生不同的冶金现象。为了定量评价不同工艺组合下的缺陷演化规律, 在 SLM 研究的历史进程中, 科研工作者

逐步发展了线能量密度 ( $E_{\text{line}}, \text{J} \cdot \text{mm}^{-1}$ )<sup>[31,36-39]</sup>、面能量密度 ( $E_{\text{Specific}}, \text{J} \cdot \text{mm}^{-2}$ )<sup>[40-43]</sup>、体积能量密度 ( $E, \text{J} \cdot \text{mm}^{-3}$ )<sup>[34,44-46]</sup> 及无量纲等效能量密度 ( $E_0^*$ )<sup>[47]</sup> 等参数, 它们的表达式分别为

$$E_{\text{line}} = q/v, \quad (1)$$

$$E_{\text{Specific}} = \frac{q}{vD} \text{ or } E_{\text{Specific}} = \frac{q}{vh}, \quad (2)$$

$$E = \frac{q}{vhl}, \quad (3)$$

$$E_0^* = \frac{Aq}{2vhl} \cdot \frac{1}{\rho C_p (T_m - T_0)}, \quad (4)$$

式中:  $q$  为激光功率;  $v$  为扫描速度;  $l$  为层厚;  $D$  为光

斑直径 ( $D=2R, R$  为光斑半径);  $h$  为搭接间距;  $A$  为粉末材料的表面吸收系数;  $\rho$  为材料的密度,  $\text{kg} \cdot \text{m}^{-3}$ ;  $C_p$  为材料的比热容,  $\text{J} \cdot \text{kg}^{-1} \cdot \text{K}^{-1}$ ;  $T_m$  为材料的熔点,  $\text{K}$ ;  $T_0$  为基板预热温度或粉末温度,  $\text{K}$ 。

笔者在总结 SLM-316L 实验数据的基础上也兼顾了其他材料, 对上述各能量密度下的致密度演化规律进行了总结, 如图 2 所示<sup>[45,48-60]</sup>。可以发现, 所有能量密度指标下的致密度均表现出相似的变化趋势, 即: 随着能量密度的增加, 致密度提高。这表明存在一个最小阈值使得零件是近乎完全致密的。不同工艺参数组合下  $E_{\text{line}}, E_{\text{Specific}}, E$  和  $E_0^*$  的范围分别为  $0.1 \sim 3.0 \text{ J} \cdot \text{mm}^{-1}$ 、 $2.0 \sim 15.0 \text{ J} \cdot \text{mm}^{-2}$ 、 $30.0 \sim 300.0 \text{ J} \cdot \text{mm}^{-3}$  和  $1.0 \sim$

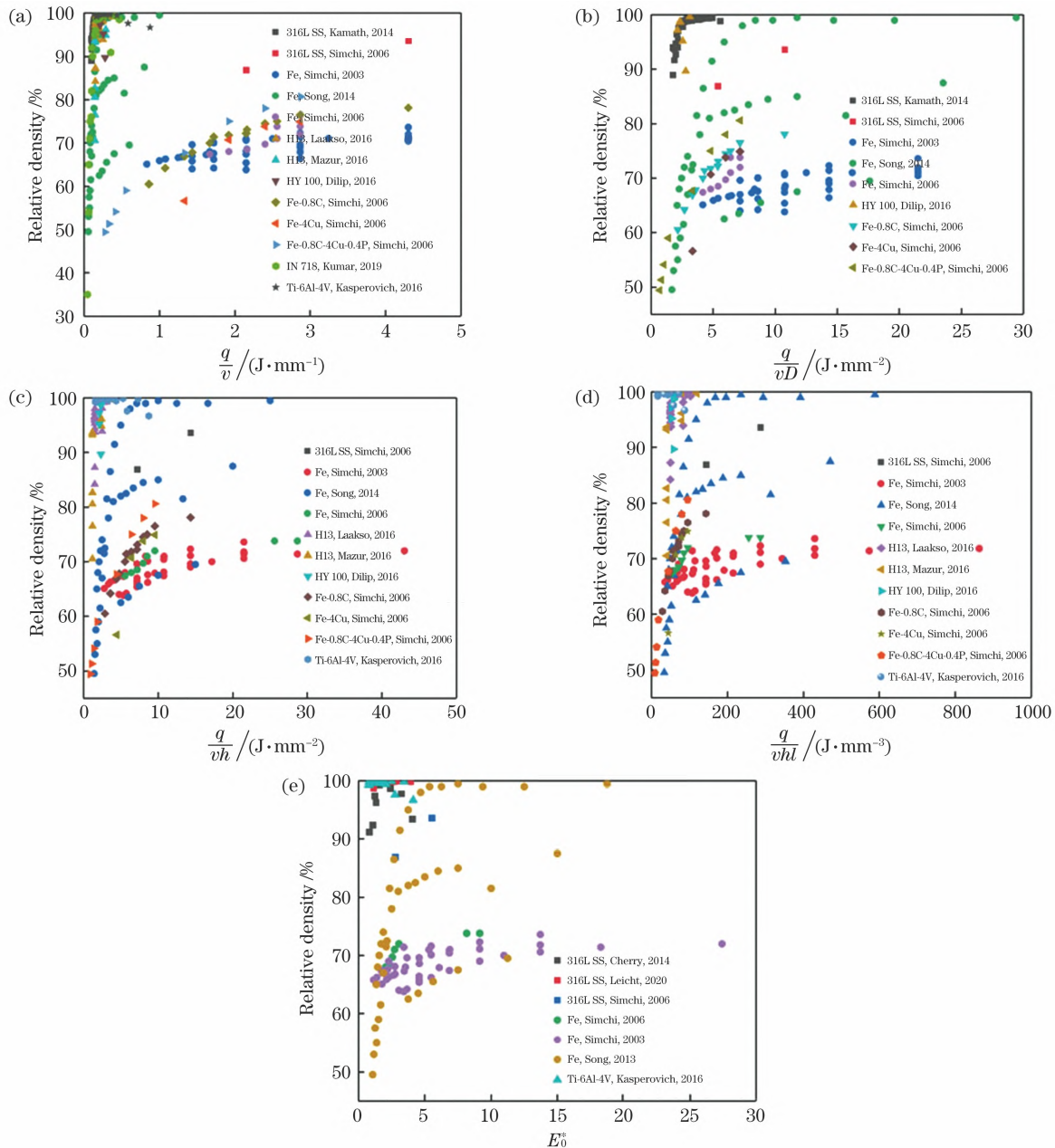


图 2 几种能量密度指标对 SLM 成形材料致密度的影响 (图中实验数据来自文献[45,48-57], 计算能量密度用到的热物性参数来自文献[58-60])

Fig. 2 Effects of several energy density indicators on relative density of selective laser melted materials (experimental data in the figures are collected from references [45, 48-57] and the thermo-physical parameters used to calculate energy density indicators are collected from references [58-60])

10.0。值得注意的是,由于  $E_0^*$  中包含了材料的热物性参数,因此若要成形致密度达 99% 以上的零件,不同工艺参数组合下的  $E_0^*$  值必须大于 1.0,如图 2(e) 所示。但  $E_0^*$  并没有考虑扫描策略、热历史及粉末的相关特性(如松装密度、单个粉末颗粒内部已存在的孔隙缺陷等),而这些因素对致密度也是有影响的<sup>[47,61-62]</sup>,这可能是等  $E_0^*$  条件下致密度不同的原因之一。

### 2.3 与零件致密度相关的几个无量纲数

随着研究的深入,人们试图发展具有普适性的度量指标,用以表征不同工艺参数对成形件致密度的影响。这些无量纲参数包括欠熔指数<sup>[30]</sup> ( $L_F$ )、无量纲加热深度比<sup>[8]</sup> ( $R_{HD}$ )、多道熔化效率数  $\eta_m$ <sup>[58]</sup>、多道蒸发效率数  $\eta_v$ <sup>[58]</sup>、 $E_{NED}$  与  $Ke_m L_d^*$  数<sup>[59]</sup>。  $L_F$  的表达式为

$$L_F = d_p / l, \quad (5)$$

式中:  $d_p$  为熔池穿透深度;  $l$  为层厚或前一沉积层的高度。  $R_{HD}$  的表达式为

$$R_{HD} = \sqrt{4\alpha(D/v)} / l, \quad (6)$$

式中:  $\alpha$  为材料熔点下对应的热扩散系数,单位为  $m^2 \cdot s^{-1}$ 。  $\eta_m$  的表达式为

$$\eta_m = \frac{Aq}{hlv\rho C_p (T_m^{eff} - T_0)}, \quad (7)$$

式中:  $T_m^{eff} = T_m + L_m / C_p$ , 其中  $L_m$  为熔化潜热。  $\eta_v$  的表达式为

$$\eta_v = \frac{Aq}{hlv\rho C_p (T_v^{eff} - T_0)}, \quad (8)$$

式中:  $T_v^{eff} = T_v + (L_m + L_v) / C_p$ , 其中  $T_v$  为材料沸点,  $L_v$  为蒸发潜热。  $E_{NED}$  和  $Ke_m L_d^*$  数的表达式分别为

$$E_{NED} = \frac{Aq}{vhl} \cdot \frac{1}{\rho C_p (T_m - T_0)}, \quad (9)$$

$$Ke_m L_d^* = \frac{Aq}{(T_m - T_0) \pi \rho C_p v R^2}. \quad (10)$$

$E_{NED}$  与  $E_0^*$  仅存在系数上的差异。

笔者计算了几种无量纲参数对致密度的影响,计算结果如图 3 所示。可以看出,不同设备、材料及工艺参数下的致密度随几种无量纲参数的增加均呈现增大的趋势,若无量纲参数过大,材料的致密度会进一步降低。当使用这些无量纲参数作为量化工具进行工艺参数的优化进而获得高致密度零件时,不同工艺参数组合下的  $R_{HD}$ 、 $\eta_m$ 、 $\eta_v$  及  $Ke_m L_d^*$  的最小值分别为 1.2、2.6、0.45 及 2.0。

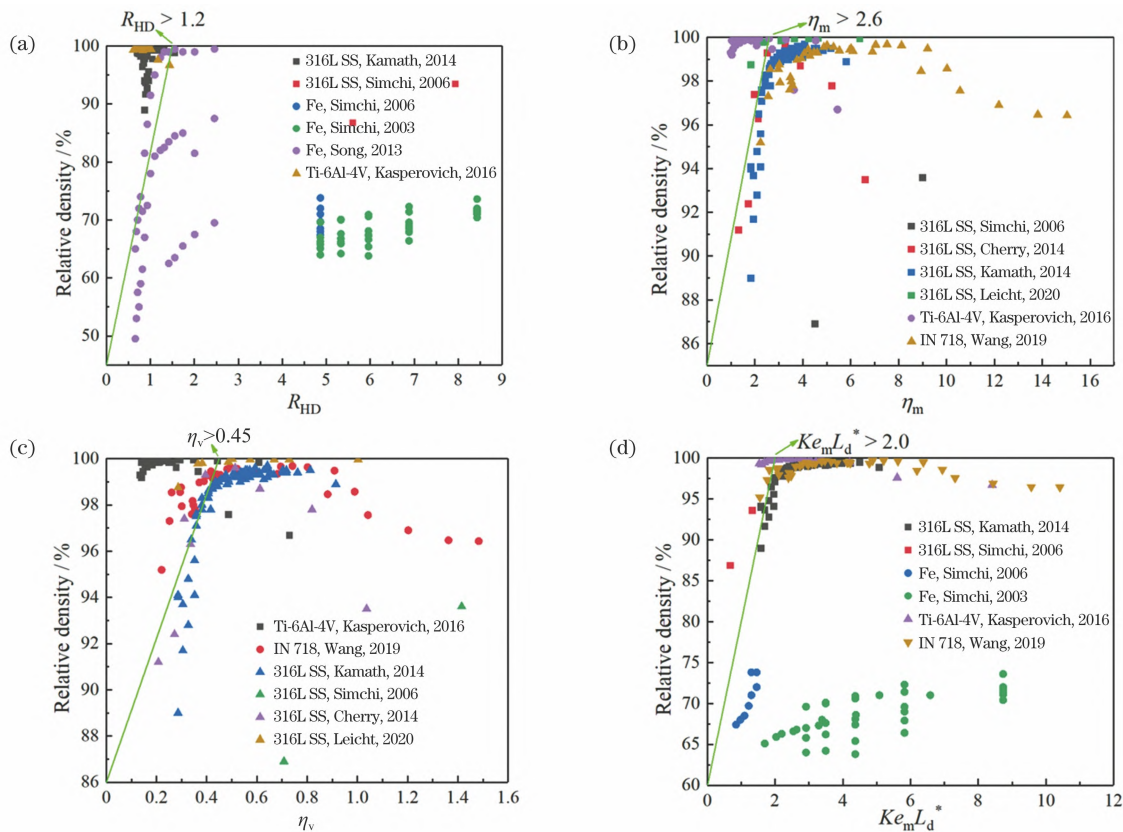


图 3 几种无量纲数对 SLM 成形材料致密度的影响(图中实验数据来自文献[45,48-51,56-58],计算无量纲数用到的热物性参数数据来自文献[58-60])

Fig. 3 Effects of several dimensionless numbers on relative density of selective laser melted materials (experimental data in the figures are collected from references [45, 48-51, 56-58] and the thermo-physical parameters used to calculate the dimensionless numbers are collected from references [58-60])

### 3 SLM-316L 不锈钢微观组织的研究现状

Zhong 等<sup>[19]</sup>从层级结构这一角度对 SLM-316L 进行了详细的微观结构表征,结果表明,成形件内部的宏观、微观及纳观结构分别由激光扫描后形成的百微米级熔池[如图 4(a)所示]、晶粒内特征尺度约为  $0.5 \mu\text{m}$  的胞状网络结构[如图 4(b)所示]以及成形过程中原位形成的富硅纳米氧化物颗粒等组成[如图 4(c)所示]。美国劳伦斯利弗莫尔国家实验室的 Wang 等<sup>[24]</sup>发表在 *Nature Materials* 上的文章指出,

SLM-316L 打印件内部形成了跨越 6 个数量级的非均匀层级结构,这种结构包括晶粒、熔池、胞结构、局部取向差、胞壁、纳米氧化物颗粒等。可以看出,SLM-316L 的层级结构由多尺度结构组成,它们之间具有包含与被包含的关系,即以特征尺寸最大的熔池为基本单元,在熔池内晶粒沿着热梯度最大的方向生长,每个晶粒内部都由许多胞结构组成,最小的纳米氧化物颗粒则随机分布于熔池内。这种结构与传统方法<sup>[63-65]</sup>制备的梯度层级结构明显不同,却也能同时提高材料的强度和韧性,这是增材制造材料性能得以大幅提高的重要原因。

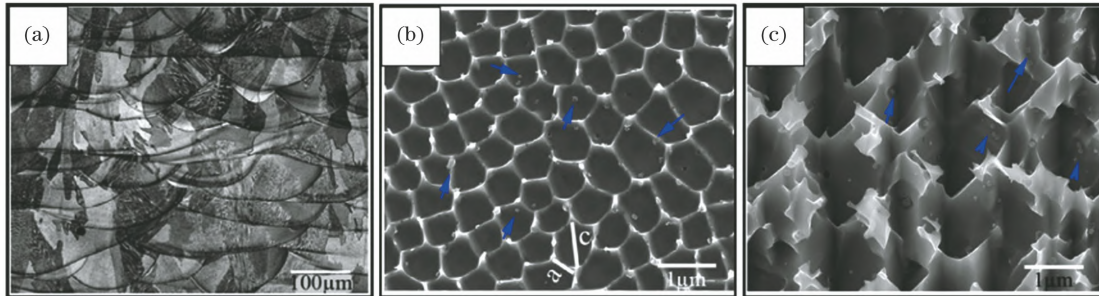


图 4 SLM-316L 的微观组织<sup>[19]</sup>,其中蓝色箭头指示纳米氧化物颗粒。(a)熔池;(b)胞结构;(c)纳米氧化物颗粒

Fig. 4 Microstructures of selective laser melted 316L sample<sup>[19]</sup>, where nano-inclusions are indicated by the blue arrows.

(a) Melt pool; (b) cell structure; (c) nano-inclusions

#### 3.1 SLM-316L 熔池的研究现状

##### 3.1.1 能量密度对熔池形貌的影响

熔池作为最基本的“重叠单元”,其形状及稳定性对 SLM 成形件缺陷和微观组织演化具有重要影响<sup>[66]</sup>。在熔池演化规律的研究中,研究人员早期采用金相法通过观察材料凝固后的横截面来获取熔池的形态<sup>[25,28,67-69]</sup>,随后逐步发展成采用原位高速 X 射线成像和衍射技术实时监测 SLM 的熔化过程<sup>[70-72]</sup>。Ma 等<sup>[25]</sup>发现,随着面能量密度的增加,SLM-316L 熔池的深宽比呈递增的趋势,如图 5(a)、(b)所示;然而,Kurzynowski 等<sup>[73]</sup>发现,随着体积能量密度的增加,SLM-316L 熔池的深宽比降低,如图 5(c)、(d)所示。这说明使用面能量密度或体积能量密度衡量熔池的形貌演化规律存在一定的局限性。Bertoli 等<sup>[74]</sup>的研究

结果表明:随着体积能量密度的增大,熔宽和熔深增加,熔高降低,且由于“Plateau-Rayleigh”不稳定性,熔高的测量有较大的不确定性,如图 6 所示。当功率一定时,随着扫描速度增大,熔池的高宽比增大,接触角增加,熔体的浸润性变差,由“Plateau-Rayleigh”不稳定驱动的表面能最小化现象越来越明显,导致熔池横截面的轮廓从相对平坦的形貌演化为高而窄的形貌[如图 6(b)所示]。熔池形貌发生变化后,熔池内的对流、传热、传质机制也会发生显著变化,进而影响最终成形件的力学性能<sup>[75-76]</sup>。考虑到功率的大小直接决定了熔池的峰值温度<sup>[77]</sup>,因此,笔者研究了等能量密度和变能量密度参数组合在低功率( $95 \text{ W}$ ,  $q^* = 20.99$ )、中等功率( $206 \text{ W}$ ,  $q^* = 45.52$ )及高功率( $360 \text{ W}$ ,  $q^* = 79.54$ )条件下的熔池演化规律,结果如图 7 所

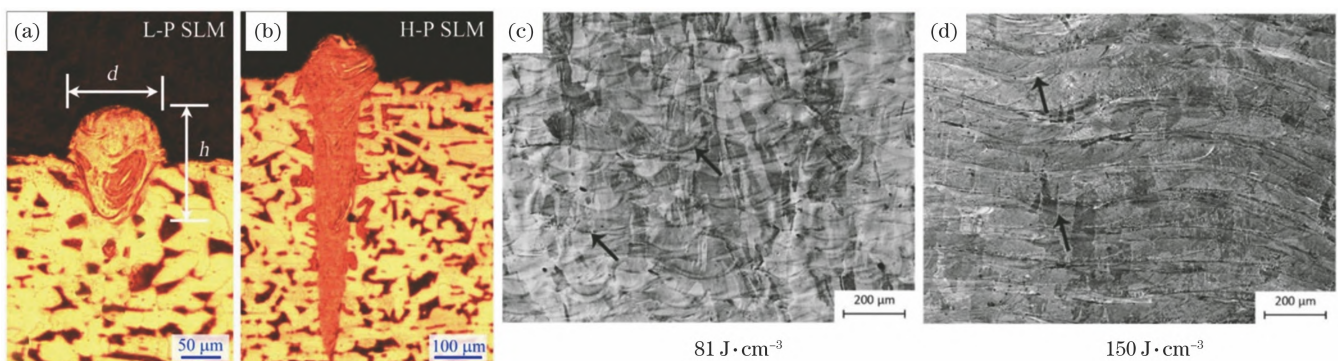


图 5 不同能量密度下的熔池形貌。(a)(b)不同面能量密度下的熔池形貌<sup>[25]</sup>;(c)(d)  $81 \text{ J}/\text{cm}^3$  和  $150 \text{ J}/\text{cm}^3$  体积能量密度下的熔池形貌<sup>[73]</sup>

Fig. 5 Melt pool shape at various energy densities. (a)(b) Melt pool morphologies at different area energy densities<sup>[25]</sup>; (c)(d) melt pool morphologies at volume energy density of  $81 \text{ J}/\text{mm}^3$  and  $150 \text{ J}/\text{mm}^3$ , respectively<sup>[73]</sup>

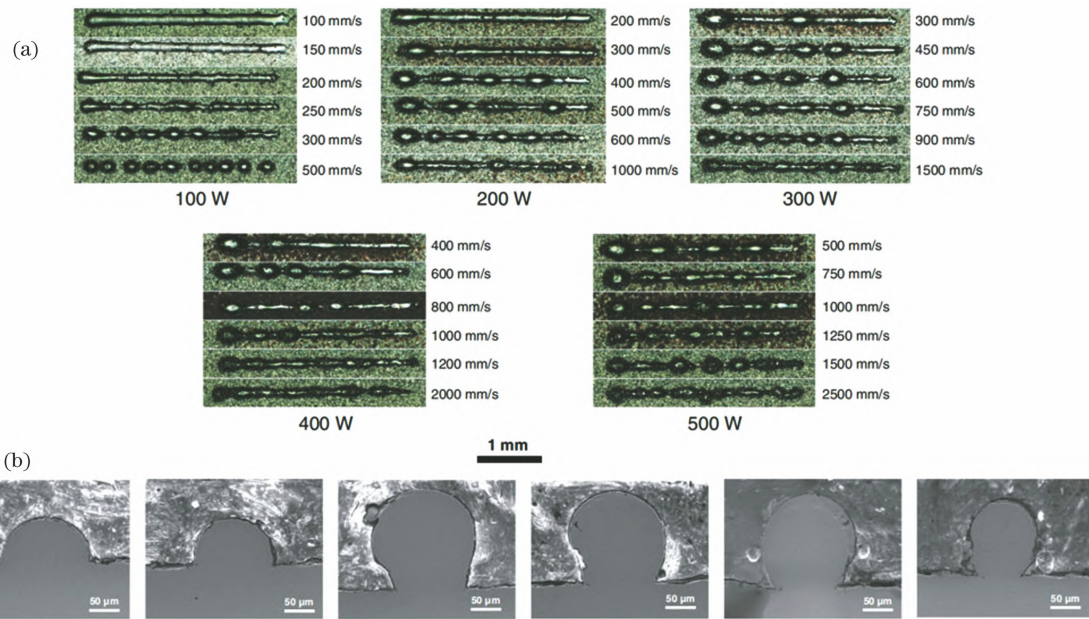


图 6 不同体积能量密度下的单道成形形貌<sup>[74]</sup>。(a) 顶面; (b) 横截面

Fig. 6 Single tracks morphologies at different volume energy densities<sup>[74]</sup>. (a) Top views; (b) cross-sectional views

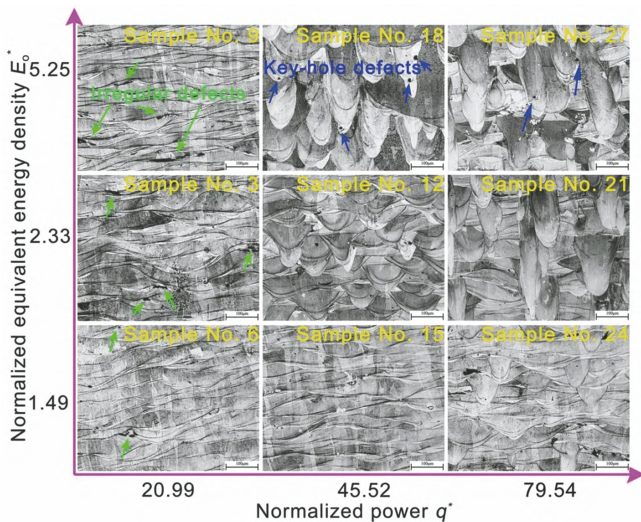


图 7 不同工艺参数下的熔池形貌(深蓝色箭头表示匙孔缺陷, 绿色箭头表示不规则缺陷)<sup>[26]</sup>

Fig. 7 Melt pool morphologies at various process parameters (dark blue arrows indicate keyhole defects, while the green ones represent irregular defects)<sup>[26]</sup>

示。观察图 7 可以发现: 在低功率条件(95 W)下, 熔池长而浅, 在高功率条件(360 W)下, 熔池窄而深; 当  $E_0^*$  不变时, 随着功率增大, 熔池的深度增大; 在功率不变的条件下, 随着  $E_0^*$  增加, 熔池深度呈增加的趋势。此外, 从图 7 中还可以看出不同功率下的熔池形貌在  $E_0^*$  相等时也存在很大差异, 这也从侧面验证了等  $E_0^*$  值下成形件的致密度也会不同, 如图 2(e) 所示。

### 3.1.2 熔池形貌对 SLM-316L 晶体结构的影响

激光功率<sup>[35,78]</sup>、扫描策略<sup>[79-80]</sup>等都可能对 SLM-

316L 材料结构的形成产生影响。Niendorf 等<sup>[78]</sup>研究了两种激光功率(400 W 与 1000 W)对 SLM-316L 成形件结构、力学性能的影响, 结果发现, 低功率条件下形成了  $\langle 011 \rangle$  结构, 而高功率条件下形成了  $\langle 001 \rangle$  结构。这项研究认为强  $\langle 001 \rangle$  结构对 SLM-316L 力学性能是不利的, 会导致材料的拉伸性能降低。Montero-Sistiaga 等<sup>[35]</sup>的研究也得到了类似的结论。研究证实, 通过调整熔池形态可以控制结构的形成<sup>[14,81-82]</sup>。新加坡南洋理工大学的 Sun 等<sup>[14]</sup>采用低功率 ( $< 400$  W) 的高斯激光束和高功率(400~1000 W)的平顶光束调控熔池形态, 结果发现: 低功率(380 W)下的高斯光束产生的熔池浅而宽, 而高功率(950 W)下的平顶光束产生的熔池窄而深, 如图 8(a)~(f) 所示, 而且浅而宽的熔池易于形成  $\langle 001 \rangle$  结构, 窄而深的熔池易于形成  $\langle 011 \rangle$  结构。 $\langle 011 \rangle$  结构比  $\langle 001 \rangle$  结构更容易激活变形孪晶, 特别是更有利于纳米孪晶的形成, 因而能够在高应变下持续变形, 提高材料的综合力学性能。因此, Sun 等认为利用合适的扫描策略和特定的激光功率来调控熔池形态是设计晶体结构的关键<sup>[14]</sup>。日本大阪大学的 Sun 等<sup>[82]</sup>采用两种工艺参数组合使材料的熔化模式分别为热传导和匙孔, 结果发现: 匙孔模式下的晶体生长方向为  $\langle 011 \rangle$ , 而在热传导模式下形成了沿  $\langle 001 \rangle$  与  $\langle 011 \rangle$  方向交替生长的晶体层片状结构, 如图 8(g)~(h) 所示, 这种结构可以大幅提高材料的耐蚀性与拉伸性能。

以上研究表明, 通过控制工艺参数可以设计不同的晶体学结构, 进而充分挖掘 SLM-316L 材料的力学性能。

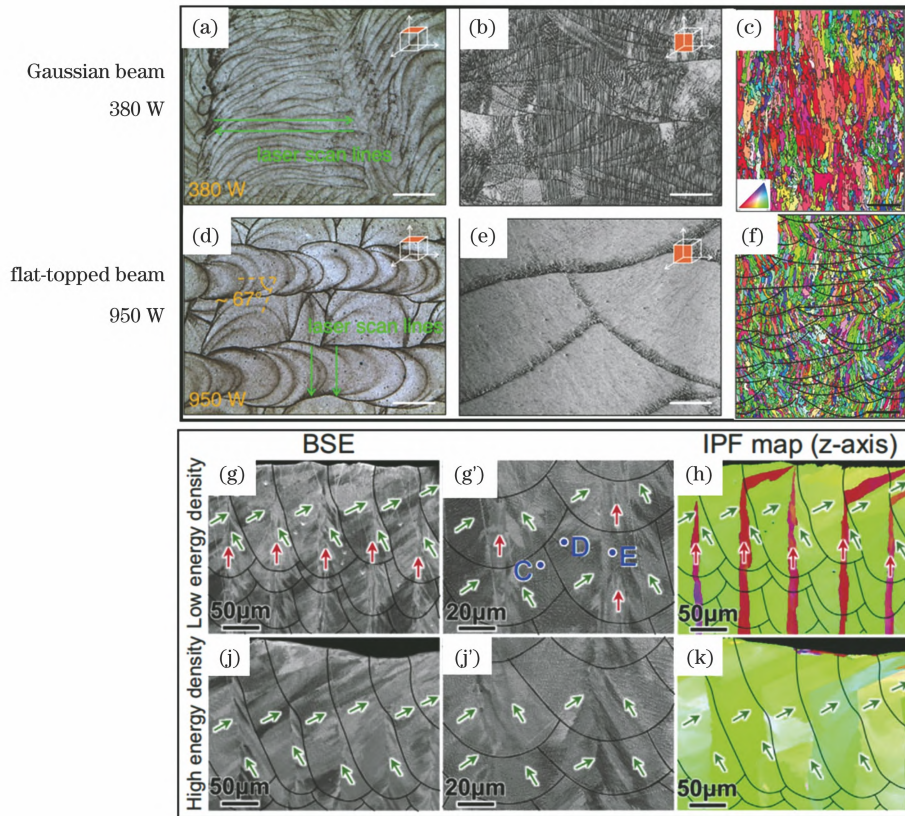


图 8 通过调控熔池形状控制织构。(a)~(f)不同激光光束和激光功率下的熔池形貌及织构<sup>[14]</sup>;(g)~(k)低能量密度与高能量密度下的熔池形貌及织构<sup>[82]</sup>

Fig. 8 Texture control by modulation of melt pool morphologies. (a)–(f) Melt pools and textures under different laser beams and laser powers<sup>[14]</sup>; (g)–(k) melt pools and textures observed in the specimens fabricated with low and high energy densities<sup>[82]</sup>

### 3.1.3 SLM 熔池尺寸的无量纲表达式研究

Wang 等<sup>[58]</sup>利用量纲分析方法对控制 SLM 物理过程的能量方程进行无量纲化,得到了高斯光束下的熔池尺寸仅与无量纲参数  $\theta_v$  有关,并给出了熔池尺寸的无量纲表达式:无量纲熔池宽度为  $W/D = B_w \sqrt{\ln(\zeta\theta_v)}$ ,无量纲熔池深度为  $d_{total}/(2R) = \zeta\theta_v$ ,其中  $W$  为熔池宽度, $d_{total}$  为熔池总深度(熔池高度+熔池深度), $\theta_v = \frac{1.37Aq}{R\rho C_p (T_v^{eff} - T_0)\sqrt{\pi R v \alpha}}$ ,有效沸点  $T_v^{eff} = T_v + (L_m + L_v)/C_p$ , $L_m$  与  $L_v$  分别为熔化潜热与汽化潜热, $T_v$  为材料的沸点,常数项  $B_w$  的拟合值为 2, $\zeta$  的拟合值为 0.814。

Gan 等<sup>[59]</sup>针对 SLM 过程中的匙孔现象,利用量纲分析给出了描述 SLM 成形过程中材料熔化模式从热传导向匙孔转变的标度律,这项研究认为熔池深宽比( $e^* = e/R$ , $e$  为熔池深度)仅与匙孔数( $Ke$ )有关。熔池深宽比和匙孔数的表达式分别为

$$e^* = 0.4(Ke - 1.4), \quad (11)$$

$$Ke = \frac{Aq}{(T_m - T_0)\pi\rho C_p \sqrt{\alpha v R^3}}. \quad (12)$$

此外,这项研究也给出了 SLM 材料不同熔化模式的判据,即

$$\begin{cases} \text{conduction mode: } e^* = 0 \text{ or } Ke < 1.4 \\ \text{transition mode: } e^* \leq 2 \text{ or } 1.4 \leq Ke < 6.0. \\ \text{keyhole mode: } e^* > 2 \text{ or } Ke > 6.0 \end{cases} \quad (13)$$

## 3.2 SLM-316L 晶粒、胞结构、位错密度及纳米氧化物颗粒的研究现状

### 3.2.1 晶粒形态及尺寸

打印态 SLM-316L 的晶粒呈各向异性的特点,即晶粒在平行于打印方向的平面上为外延生长的柱状晶结构,而在垂直于打印方向的平面上为“棋盘”状等轴结构<sup>[35,69,83-85]</sup>。出现这种微观结构的主要原因是:在 SLM 成形过程中,粉末材料的快速熔化与凝固是远离平衡条件的,晶粒总是沿着最大温度梯度的方向生长<sup>[14,34,82]</sup>。晶粒的各向异性特点导致了 SLM-316L 力学性能的各向异性行为,即,通常情况下沿水平方向打印的试样比沿垂直方向打印的试样强度高 10% 左右<sup>[86-87]</sup>。SLM-316L 晶粒尺寸与工艺参数有关:Ma 等<sup>[25]</sup>研究了面能量密度对晶粒宽度和长度的影响,结果发现,随着面能量密度的增加,晶粒宽度、晶粒长度和晶粒长宽比均呈单调递增的趋势;Montero-Sistiaga 等<sup>[35]</sup>使用 400 W 高斯激光与 1000 W 平顶激光研究了 SLM-316L 晶粒的演化规律,同样发现高能量密度下的

晶粒尺寸更加粗大。表 1 总结了不同文献中的晶粒尺寸数据,可以看出,SLM-316L 打印态材料通常比传统方法制备的 316L 材料的晶粒尺寸更粗大,其晶粒长度通常为几十到几百微米,而晶粒宽度一般小于 100  $\mu\text{m}$ 。

表 1 不同文献中 SLM-316L 的晶粒尺寸

Table 1 Grain size of selective laser melted 316L samples in different references

Author and reference	Power / W	Scanning speed / ( $\text{mm}\cdot\text{s}^{-1}$ )	Aspect ratio	Grain width / $\mu\text{m}$	Grain length / $\mu\text{m}$
Shamsujjoha, <i>et al.</i> [89]	400	—	—	—	200
Montero-Sistiaga, <i>et al.</i> [35]	400	—	1.4	70	100
Montero-Sistiaga, <i>et al.</i> [35]	1000	—	10	~100	~1000
Sun, <i>et al.</i> [14]	380	—	—	13.2	—
Sun, <i>et al.</i> [14]	950	—	—	11.6	—
Ma, <i>et al.</i> [25]	200–2000	800–2200	5–15	16–27	120–400
Wang, <i>et al.</i> (concept) [24]	150–350	700–1700	—	45	—
Wang, <i>et al.</i> (Fraunhofer) [24]	296–353	150–225	—	20	—
Voisin, <i>et al.</i> [90]	150	700	—	9	—
Salman, <i>et al.</i> [91]	175	688	—	45	—
Chen, <i>et al.</i> [84]	200	850	—	5.9	—
Sistiaga, <i>et al.</i> [92]	—	—	—	—	100
Saeidi, <i>et al.</i> [15]	195	800	—	—	10–100
Jiang, <i>et al.</i> [83]	206	900	1.6	41.2	67.9
Khodabakhshi, <i>et al.</i> [93]	—	—	—	7.5	—

### 3.2.2 胞结构的研究现状

目前,大部分研究者认为非均匀层级结构是 SLM-316L 不锈钢获得高强度、高韧性的主要原因,而 SLM-316L 不锈钢的屈服强度较传统材料大幅提高的主要原因是晶粒内部形成了非常细小的位错胞结构<sup>[19,24,34]</sup>。关于 SLM-316L 不锈钢材料中胞结构的形成机理目前尚未形成共识,主要有如下几种观点:

1)从凝固理论和热力学角度看,胞结构的形成可以用成分过冷理论及界面稳定性理论解释<sup>[19,94]</sup>。成分过冷理论强调了热力学在决定凝固组织形态方面的重要性,认为微观结构从平面晶形态转变为胞状形态或树枝晶形态取决于温度梯度  $G$  与凝固速率  $R$  之比(即  $G/R$ );而界面稳定性理论认为合金微观组织的形态取决于与被加工合金相关的界面动力学和传热方面的特性,微观结构的形态取决于凝固前沿的速度和固/液界面俘获溶质的能力<sup>[95]</sup>。SLM 过程中的温度梯度及凝固速率都比较大,导致 SLM 材料中的胞状树枝晶优先于平面晶生长,因此在组织中观察到了胞状结构<sup>[19,24]</sup>。

2)从流体力学的角度看,Prashanth 等<sup>[96]</sup>认为上述理论不能解释 SLM 与传统成形过程的差异。SLM

大量的拉伸测试结果已表明 SLM-316L 材料的拉伸强度远高于传统制备方法得到的 316L 材料的拉伸强度<sup>[14,24,88-89]</sup>,这也间接证明了决定 SLM-316L 屈服强度的主要因素可能不是由大角度晶界确定的晶粒尺寸。

的熔池尺度非常小,在高温梯度下会形成强烈的 Marangoni 流动,从而导致溶质积累。由于熔池至少有一面与固体物质接触,熔池的一面或两面被粉末颗粒包围,熔池顶部又与保护气体接触,这种熔融环境使得熔池内部温度的不均匀性增强,导致由表面张力效应引起的热毛细对流作用增强,产生强烈的涡流,因此熔池凝固形成复杂的胞状结构<sup>[97]</sup>。Prashanth 等<sup>[96]</sup>认为 SLM 材料中复杂的胞结构是由表面张力驱动的不稳定性导致的,将其称为“Benard Marangoni Surface Instability”(BMI 表面不稳定)<sup>[97]</sup>,并给出了 SLM 材料形成胞结构的 4 个条件。

3)Birnbbaum 等<sup>[98]</sup>基于金属材料位错胞的形成与应力/应变能场有关这一事实<sup>[99]</sup>,结合 SLM 成形时会在凝固后的材料中产生很大的残余应力<sup>[20,100]</sup>,认为 SLM 始终经历连续堆叠的循环热作用,这使得 SLM 过程中材料的屈服强度相较室温下的屈服强度显著降低,导致材料阻碍位错运动的能力降低。位错在高残余应力驱动下更容易发生运动,从而促进了位错结构的动态演化。这项研究认为 SLM-316L 产生的热应变和材料屈服应力在循环热作用下的降低共同导致了胞结构的形成。

4)Bertsch 等<sup>[101]</sup>通过改变制备样品的几何约束



(即“1D”杆、“2D”薄壁和“3D”块体)来控制成形件中的热应力,系统地研究了增材制造不锈钢中位错胞结构的起源。结果表明:成形过程中胞状树枝晶的微偏析、沉淀物或局部取向差会影响位错结构的组织方式,但它们并不是胞结构形成的主要原因。胞结构起源于打印过程中受约束的介质由于热膨胀/热收缩而发生的变形,而这些变形主要是由熔池周围的约束和热循环决定的。可以通过调整工艺参数来控制位错结构的发展和位错密度的特征,这些工艺参数包括冷却速率、热梯度、搭接间距、层厚、熔池穿透深度等。

研究表明,提高输入到熔池中的面能量密度<sup>[25]</sup>、降低扫描速度<sup>[88]</sup>、增大体积能量密度<sup>[24,34]</sup>均会增大胞结构的尺寸。笔者的研究结果表明,虽然不同工艺下

试样的胞结构体积分数有较大差异,但胞结构的尺寸随着输入到粉末床的能量密度增加大致呈增大的趋势,如图 9(a)所示,这主要是由熔池内冷却速率的降低导致的<sup>[24-25,34,88]</sup>。同时,当  $E_0^*$  低于 3.24 时(对应于体积能量密度为  $117 \text{ J} \cdot \text{mm}^{-3}$ ),不同工艺下的胞结构的尺寸差异较小(胞结构的尺寸介于  $0.35 \sim 0.5 \mu\text{m}$  之间)。根据 Wang 等<sup>[24]</sup>的研究,决定 SLM-316L 材料屈服强度的微结构主要是胞结构尺寸而非晶粒尺寸,因此,采用较低的能量密度参数组合获得高密度且胞结构尺寸较为细小的零件是获得优异力学性能的一条可能途径<sup>[26]</sup>。笔者所在团队利用低于大多数文献中的能量密度参数组合验证了这条途径的正确性,如图 9(b)所示。

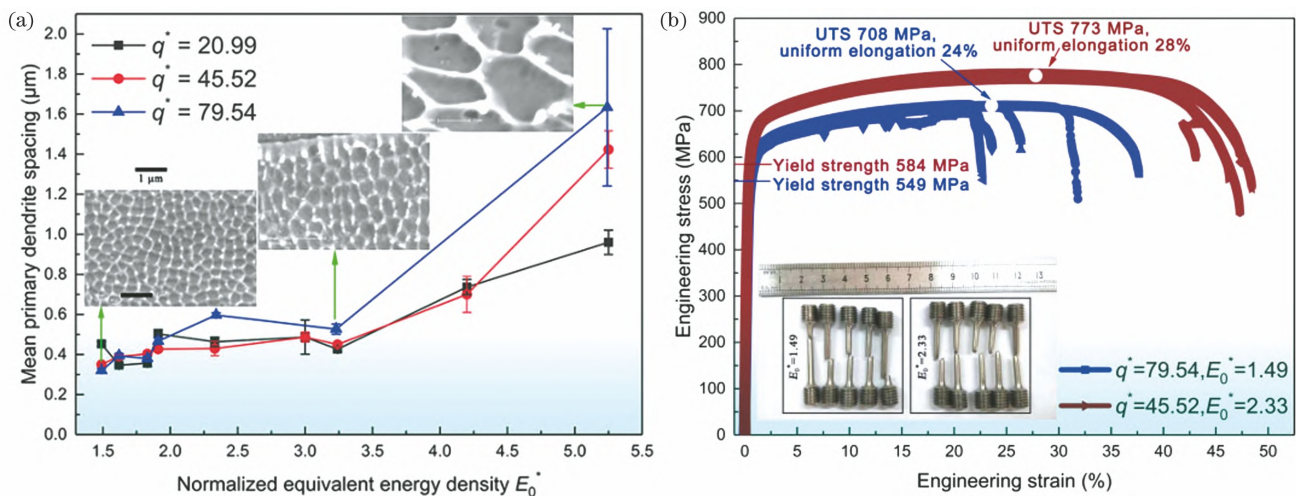


图 9 工艺参数对 SLM-316L 不锈钢胞结构及拉伸性能的影响<sup>[26]</sup>。(a)工艺参数对胞结构尺寸的影响;(b)低能量密度下的工程应力-应变曲线

Fig. 9 Effect of process parameters on cellular structure and tensile property of an selective laser melted 316L stainless steel<sup>[26]</sup>.

(a) Effect of process parameters on cellular structure size; (b) engineering stress-strain curves at low energy density

### 3.2.3 SLM-316L 打印态材料的位错密度及原位形成的纳米氧化物颗粒

打印态 SLM-316L 的胞壁上存在大量的位错结构<sup>[24,88,90]</sup>,这种结构与传统方法使用强烈塑性变形后得到的微结构很相似<sup>[102-103]</sup>。关于 SLM-316L 这种位错胞结构的起源问题上述已有讨论<sup>[19,94,96,98,101]</sup>,研究人员为了回答位错胞结构对材料力学性能的影响机理,利用 Williamson 和 Hall<sup>[104]</sup>提出的衍射峰宽化模型估算了成形件的位错密度,结果表明,打印态 SLM-316L 位错密度的量级为  $10^{14} \sim 10^{15} \text{ m}^{-2}$ <sup>[89,105-106]</sup>。对于完全退火态的 316L 不锈钢材料,其位错密度通常介于  $10^{10} \sim 10^{11} \text{ m}^{-2}$ <sup>[9,105]</sup>,而热成形马氏体钢和循环变形奥氏体钢的位错密度分别为  $2.36 \times 10^{14} \text{ m}^{-2}$ <sup>[107]</sup>和  $1.5 \times 10^{14} \text{ m}^{-2}$ <sup>[108]</sup>。可见,打印态 SLM-316L 材料具有很高的位错密度。根据 Taylor 硬化定律<sup>[109]</sup>,位错密度对屈服强度的贡献可以表示为  $\Delta\sigma = M\alpha'G|b|\sqrt{\rho}$ ,其中  $M$  为泰勒因子, $G$  为材料的剪切模量( $74 \text{ GPa}$ <sup>[14]</sup>), $b$  为柏氏矢量(其大小为  $0.25 \text{ nm}$ <sup>[89]</sup>),

$\rho$  为位错密度, $\alpha'$  为常数。若按打印态材料内部位错密度分别为  $10^{14} \text{ m}^{-2}$  和  $10^{15} \text{ m}^{-2}$  计算,那么位错密度对流动应力的贡献分别为  $132 \text{ MPa}$  与  $417 \text{ MPa}$ ( $M\alpha'$  取值为  $0.713$ ),已经可与传统退火态 316L 的屈服强度( $170 \text{ MPa}$ <sup>[110]</sup>)比拟。打印态材料内部如此高的位错密度为位错运动提供了更多保障,因此屈服应力大幅提高。

从成形过程来讲,SLM 是在密闭舱室内逐层完成零件打印的,舱室内的氧通常控制在一定含量以下,以保证成形过程中的表面质量与内部质量。但是,舱室内仍旧会存在极少量的氧气,打印过程中合金材料中易氧化的元素(如 Si<sup>[16,21]</sup>)会优先与氧发生反应,原位形成纳米氧化物颗粒,其尺寸通常为几十纳米到几百纳米<sup>[24,111]</sup>。目前,在 SLM-316L 材料中原位形成纳米氧化物颗粒的研究已被大量报道<sup>[19,21,24,112-113]</sup>;Saeidi 等<sup>[21]</sup>的研究表明 SLM-316L 内原位形成的纳米颗粒(直径约为  $50 \text{ nm}$ )是材料拉伸变形过程中位错运动的有效屏障,他们认为这是材料取得高强度的主要原因;Wang 等<sup>[24]</sup>利用

Orowan 强化模型估算了原位形成的纳米颗粒对材料屈服强度的贡献,结果显示 Orowan 强化模型的计算值在 5~10 MPa 之间,与材料屈服强度 (>590 MPa)相差 1~2 个数量级,显然贡献不大。最近,Cui 等<sup>[114]</sup>利用 Orowan 和 Russel-Brown 两种强化模型分别估算了纳米颗粒对屈服强度的贡献,计算结果分别为 12.5 MPa 和 14.6 MPa,可以看出仍远低于打印态材料的屈服强度(556 MPa±20 MPa)。这些研究表明 SLM-316L 内原位形成的纳米氧化物颗粒对屈服强度的影响可以忽略。

## 4 SLM-316L 不锈钢的力学性能研究现状

### 4.1 硬度

SLM 成形件的硬度受孔隙率及微观组织的影响<sup>[45]</sup>。Krakhamlev 等<sup>[115]</sup>的研究结果表明,SLM-316L 的显微硬度与胞结构尺寸的均方根满足 Hall-Petch 关系,提高扫描速度(即降低输入到粉末床的能量密度)对于提高显微硬度具有积极作用。Ma 等<sup>[25]</sup>的研究也表明较低的面能量密度有利于提高成形件的显微硬度。然而,Tucho 等<sup>[16]</sup>的研究表明随着体积能量密度从  $50 \text{ J} \cdot \text{mm}^{-3}$  增加到  $80 \text{ J} \cdot \text{mm}^{-3}$ ,成形件的孔隙率逐渐降低,显微硬度逐渐升高,这与 Cherry 等<sup>[45]</sup>的研究结果基本一致,即:当体积能量密度低于  $125 \text{ J} \cdot \text{mm}^{-3}$  时,随着体积能量密度的增加,显微硬度逐渐增大,进一步提高体积能量密度,显微硬度呈下降趋势。可见:面能量密度或者体积能量密度不是决定显微硬度大小的唯一参数,显微硬度还与扫描策略、孔隙率及微观组织有关。SLM-316L 打印态样件显微硬度值的范围为  $165 \sim 325 \text{ HV}^{[16,45,92,116-118]}$ 。绝大多数研究者所获得的最大硬度值为  $220 \sim 280 \text{ HV}$ ,这一硬度值远远高于退火态材料的硬度值( $155 \sim 170 \text{ HV}^{[119]}$ )。值得注意的是,Saeidi 等<sup>[21,117]</sup>报道了一个非常高的维氏硬度值: $325 \text{ HV} \pm 5 \text{ HV}$ 。研究人员认为这是由其成形件内胞结构尺寸细小和纳米氧化物颗粒含量较多造成的<sup>[16,118]</sup>。笔者研究发现:即使是同一工艺下的成形件(致密度 >99%),当加载载荷不同时,获得的硬度值也会有显著差异(如图 10 所示):9.8 N 载荷下的显微硬度约为  $235 \text{ HV}_1$ ,而 0.98 N 载荷下的显微硬度高达  $302.42 \text{ HV}_{0.1}$ ,其中 0.98 N 载荷下的显微硬度与 Saeidi 等<sup>[21]</sup>报道的显微硬度值相当。这说明较大的载荷形成的压痕较大,可能会覆盖更多的孔隙缺陷,使其在加载过程中坍塌,降低了材料抵抗变形的能力,进行使得硬度值降低;而载荷较小时,压痕覆盖的面积小,材料的显微组织起主要作用,因而在某些局部区域可能测出较高的显微硬度。

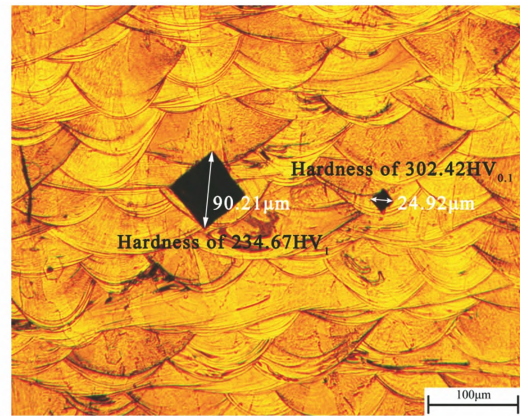


图 10 0.98 N 与 9.8 N 载荷下的典型压痕形貌<sup>[28]</sup>  
Fig. 10 Typical morphology of indent with the load of 0.98 N and of 9.8 N, respectively<sup>[28]</sup>

### 4.2 拉伸性能

位错的运动控制着金属的塑性变形,因而决定着材料的力学性能。金属材料的强度可以通过调控其微观组织进而阻碍位错的运动得到提高,如在基体中引入二次相、晶界或者其他内部界面<sup>[120]</sup>,但这种方法在提高材料强度的同时会不可避免地牺牲材料的塑性。研究表明,在材料内部引入孪晶<sup>[120-121]</sup>、梯度纳米晶<sup>[65]</sup>或者非均匀层片状结构<sup>[64]</sup>,可以在提高材料强度的同时使材料保持较高的塑性。近年来,一些研究机构<sup>[14,24,88-89]</sup>获得了强韧兼备的 SLM-316L 不锈钢打印态样件,展现了 SLM 技术制备综合力学性能优良的构件的潜力。表 2 总结了不同文献报道的打印态 SLM-316L 的拉伸性能(包括屈服强度  $\sigma_y$ 、抗拉强度  $\sigma_{\text{UTS}}$ 、均匀延伸率  $\epsilon_{\text{UE}}$  及断后延伸率  $\epsilon_f$ ),将这些数据与传统方法(冷轧、锻造等)制备的 316L 材料的力学性能进行对比,可以发现打印态 SLM-316L 的  $\sigma_y$ 、 $\sigma_{\text{UTS}}$ 、 $\epsilon_f$  值分别在  $409 \sim 680 \text{ MPa}$ 、 $509 \sim 773 \text{ MPa}$ 、 $12\% \sim 87\%$  之间,而且 SLM-316L 的  $\sigma_y$  值均高于锻件水平( $327 \text{ MPa}$ ),绝大部分  $\sigma_{\text{UTS}}$  值也高于锻件水平( $620 \text{ MPa}$ ),但  $\epsilon_f$  值的分散性较大,这可能是孔隙率、缺陷尺寸及拉伸试样尺寸不同导致的<sup>[26,34,122]</sup>。

如图 11 所示,目前,SLM-316L 高强高韧机理的主要学术观点包括凝固后形成的胞结构<sup>[19]</sup>、位错网络结构<sup>[88]</sup>、高位错密度<sup>[89,106]</sup>、晶体层片状结构<sup>[82]</sup>、纳米氧化物颗粒<sup>[21]</sup>、〈011〉织构诱导的 TWIP 效应<sup>[14]</sup> 及非均匀层片结构<sup>[24]</sup>。这些研究的共识是:通过调控工艺参数获得特定微结构的方式来制备高强高韧 SLM-316L 材料是可行的!

众所周知,材料的力学性能取决于其微观结构。对于传统方法制备的 316L 材料,其屈服强度  $\sigma_y$  与晶粒尺寸满足 Hall-Petch 关系。然而,关于 SLM-316L 材料屈服强度的预测目前还存在争议,主要有如下三种观点:

表 2 SLM-316L 拉伸性能总结(\*表示该数据是从工程应力-应变曲线中估算得到的)

Table 2 A summary of tensile properties of 316L samples produced via different selective laser melting parameters and processing technologies (\* represents the data obtained by estimating from engineering stress-strain curves)

Author and reference	$\sigma_y$ /MPa	$\sigma_{UTS}$ /MPa	$\epsilon_{UE}/\%$	$\epsilon_f/\%$
Jiang, <i>et al.</i> [26]	584±16	773±4	28±1	46±1
Shamsujjoha, <i>et al.</i> [89]	584	667	23	49
Bahl, <i>et al.</i> [105]	550	675		44
Wang, <i>et al.</i> (concept) [24]	595-680	700	34±3	58*
Wang, <i>et al.</i> (Fraunhofer) [24]	450-557	640	59	87*
Qiu, <i>et al.</i> [23]	558	686		51
Qiu, <i>et al.</i> [23]	541	681		51
Qiu, <i>et al.</i> [23]	519	663		47
Casati, <i>et al.</i> [69]	554	685		36
Zhong, <i>et al.</i> [19]	487	594		49
Saeidi, <i>et al.</i> [21]	428	654		45
Saeidi, <i>et al.</i> [21]	456	703		46
Liu, <i>et al.</i> [88]	552			83
Sun, <i>et al.</i> [14]	567	660*		40*
Wang, <i>et al.</i> [34]		590	21	
Elangeswaran, <i>et al.</i> [123]	453	573		46
Riemer, <i>et al.</i> [124]	462	565		54
Suryawanshi, <i>et al.</i> [125]	512	622		20
Suryawanshi, <i>et al.</i> [125]	430	509		12
Suryawanshi, <i>et al.</i> [125]	536	668		25
Suryawanshi, <i>et al.</i> [125]	449	528		12
Kurzynowski, <i>et al.</i> [73]	517	687		32
Kurzynowski, <i>et al.</i> [73]	463	687		25
Kurzynowski, <i>et al.</i> [73]	454	750		29
Kurzynowski, <i>et al.</i> [73]	440	662		28
Kurzynowski, <i>et al.</i> [73]	409	674		26
ASMIH Handbook Committee (hot finished+annealed) [110]	170	480		40
ASMIH Handbook Committee (cold finished+annealed) [110]	170	480		30
ASMIH Handbook Committee (cold finished) [110]	310	620		30
Segura, <i>et al.</i> (wrought 316L) [126]	327±10	620±4.5		53±0.8

1) 利用 Hall-Petch 关系式  $\sigma_y = \sigma_0 + k/\sqrt{d}$  ( $\sigma_0$  和  $k$  为 Hall-Petch 参数) 进行预测, 其中  $d$  用胞结构尺寸代替 [24];

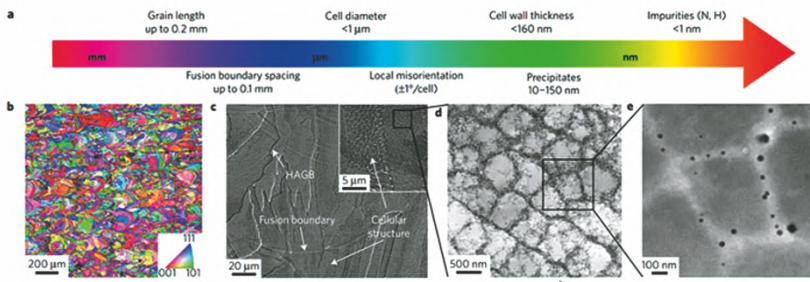
2) 在 Hall-Petch 关系式  $\sigma_y = \sigma_0 + k/\sqrt{d}$  中,  $d$  取晶粒尺寸进行估算 [25];

3) 估算打印态样件的位错密度, 然后用修正后的 Hall-Petch 关系 ( $\sigma_y = \sigma_0 + k/\sqrt{d} + M\alpha G |b| \sqrt{\rho}$ , 其中,

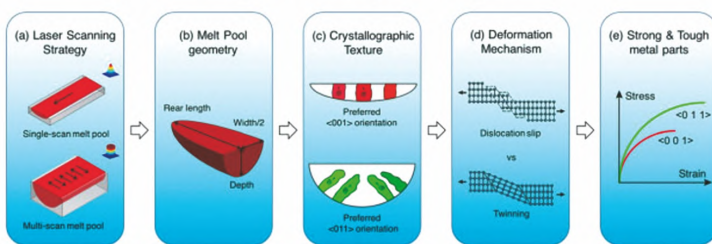
$d$  为晶粒尺寸 [105]) 进行估算。

值得注意的是, 这些屈服强度的预测方法均基于特定的工艺参数范围, 而且所使用的设备有很大差异, 而 SLM-316L 材料的微结构与成形工艺高度相关, 在特定的工艺条件下, SLM-316L 材料层级结构中的某一特定微结构 (如熔池 [14,82]、胞结构 [19,24]、位错密度 [89,106] 等) 对拉伸性能的贡献会占据主导作用, 这可

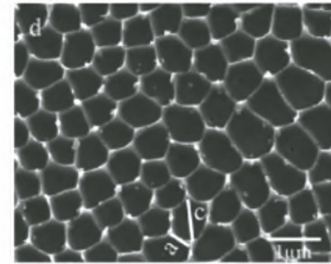
**Wang, et al. Hierarchically heterogeneous microstructure, with length scales spanning nearly six orders of magnitude.**



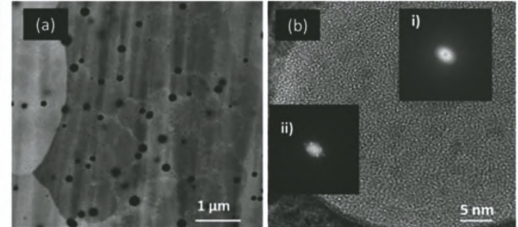
**Sun, et al. Enhancing the TWIP effect by tailoring the melt pool shape.**



**Zhong, et al. Cellular structure.**



**Seaidi, et al. Oxide nanoinclusions.**



**Liu, et al. Dislocation networks.**

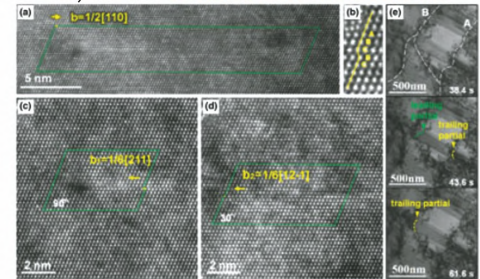


图 11 SLM-316L 高强高韧机理的学术观点总结<sup>[14,19,21,24,88]</sup>

Fig. 11 A summary of academic viewpoints on high strength and high ductility mechanisms of selective laser melted 316L stainless steel<sup>[14,19,21,24,88]</sup>

能是文献中出现多种预测方法的原因之一。

笔者认为 SLM-316L 不锈钢材料的非均匀层级结构在拉伸变形过程中作为一个整体对载荷的传递和应变的分配产生影响,因此笔者从非均匀层级结构这一角度出发,研究了 SLM-316L 的微结构在拉伸变形过程中的演变特点。结果发现:与打印态的熔池形貌相比,拉伸过程中的熔池宽度沿着加载方向被拉长,而熔池深度则沿着打印方向减小,如图 12(a)、(c)所示;胞结构在外力作用下发生严重变形,由最初的“准多边形”变为长条形,如图 12(b)、(e)所示;在百微米级尺度上可以观察到熔池发生撕裂,图 12(d)所示。熔池发生撕裂主要是由相邻熔池边界的非规则缺陷造成的,这些缺陷作为应力集中源,在外力的作用下导致材料沿着熔池边界撕裂,因而可以认为熔池边界是 SLM 成形件的“薄弱”部位之一。在几百纳米的尺度上,发现了断裂位点既可以位于胞结构处,也可以位于胞枝晶位置处,如图 12(f)所示。这说明胞结构的边界也是 SLM-316L 的“薄弱”部位之一。随着应变变量  $\epsilon$  从 15% 增大到 46%,晶粒逐渐细化,平均晶粒尺寸分别为打印态晶粒尺寸的 24% ( $\epsilon = 15\%$ )、21% ( $\epsilon = 30\%$ )、15% ( $\epsilon = 46\%$ ),如图 13 所示。这表明 SLM-

316L 在拉伸变形过程中发生了晶粒细化,打印态的粗大柱状晶在外力作用下陆续破碎,导致晶粒随着应变量的增加而逐渐减小。对于 SLM-316L 不锈钢材料,晶粒出现这种动态细化行为的可能原因之一是该材料的层错能较低(约为  $20 \text{ mJ} \cdot \text{m}^{-2}$ <sup>[14]</sup>),因此材料在变形过程中形成了形变孪晶<sup>[14,24]</sup>。事实上,材料微观组织发生这种动态细化的现象在具有“传统”非均匀梯度结构的中熵合金(CrCoNi)中曾被报道过<sup>[127]</sup>,该材料是面心立方(FCC)结构,与 316L 不锈钢的结构一致。Yang 等<sup>[127]</sup>曾指出,对于低层错能的 FCC 结构材料,其在变形过程中更易产生纳米孪晶和层错,而且可以动态地提高材料组织的非均匀性,使得材料的应变硬化率始终维持在较高的水平,因而材料强度提升的同时韧性也较高。通过研究熔池、晶粒、胞结构等发现,对这些非均匀层级结构进行拉伸变形时,随着应变的增加,晶粒变得更加细小(如图 13 所示),结构也变得更加不均匀,直至破坏之前一直在变形(如图 12 所示)。这意味着非均匀层级结构的每一部分在应力作用下“协同”变形并传递应力,使得材料在变形过程中的加工硬化周期变大,因而材料强度提升的同时塑性也在提高。

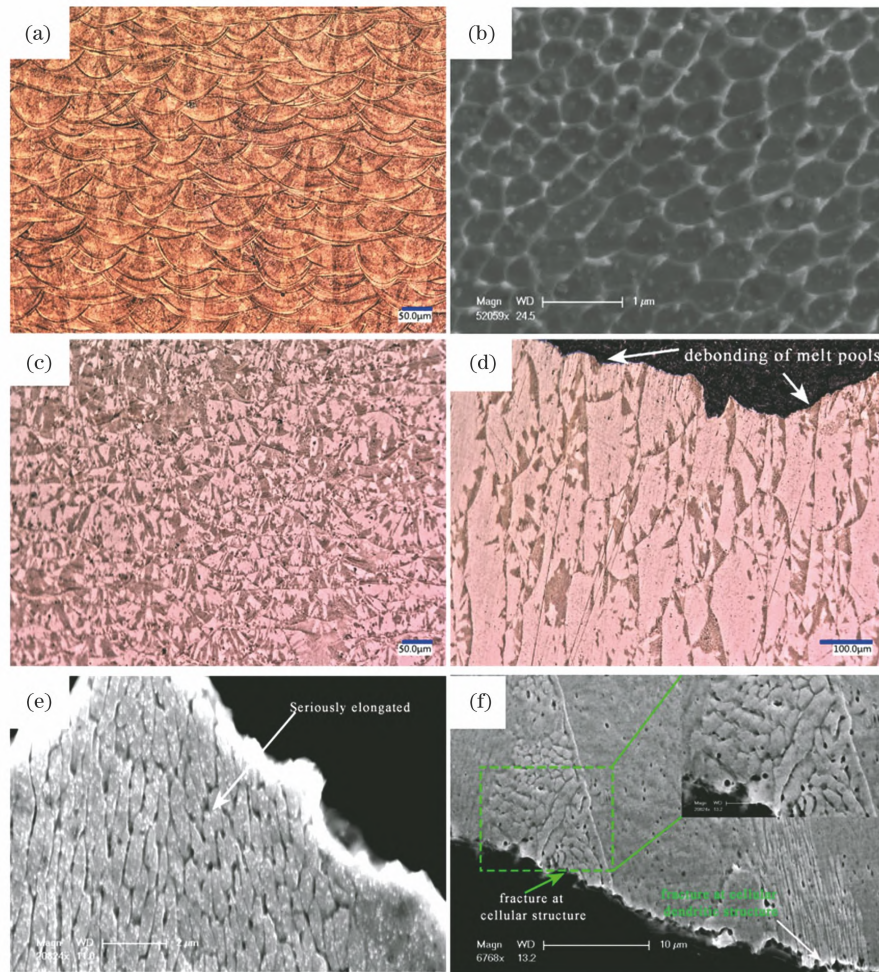


图 12 SLM-316L 的微结构。打印态 SLM-316L:(a)熔池形貌;(b)胞结构。断后 SLM-316L:(c)熔池形貌;(d) 熔池撕裂;(e)胞结构;(f)断裂发生在胞结构及胞枝晶位置处

Fig. 12 Microstructures of 316L fabricated by selective laser melting. As-built part: (a) melt pool morphology; (b) cellular structure. As-fractured samples: (c) melt pool morphology; (d) optical microscopy (OM) image showing the debonding of melt pool; (e) a high magnified scanning electron microscopy (SEM) image showing the seriously elongated cellular structure after tensile test; (f) SEM image showing the fractured location occurs at both cellular structure and cellular dendrite structure

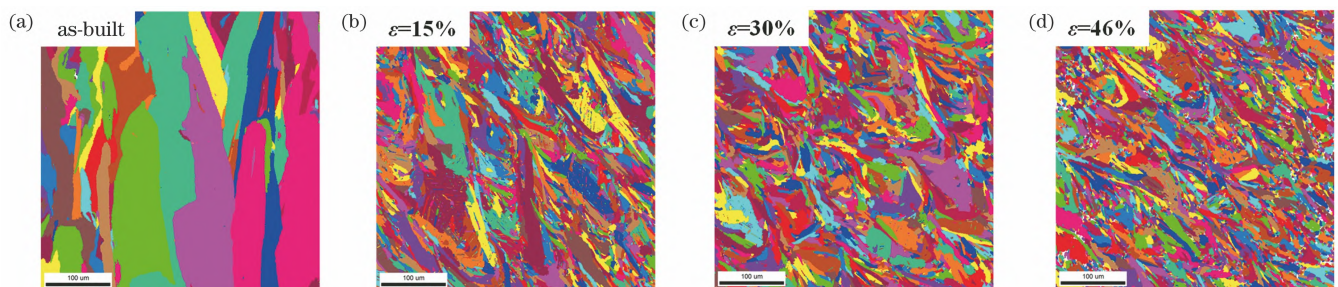


图 13 不同应变下 SLM-316L 不锈钢的晶粒形貌图。(a)打印态;(b)15%;(c)30%;(d)46%

Fig. 13 Grain maps of selective laser melted 316L stainless steel at different strain levels. (a) As-built; (b) 15%; (c) 30%; (d) 46%

### 4.3 耐蚀性

研究表明,在 SLM-316L 胞结构的胞壁上存在 Cr 和 Mo 元素的微观偏析<sup>[24,117]</sup>,溶质分布和微观结构的不均匀性会降低材料的耐蚀性<sup>[128]</sup>。与锻造 316L 相比,SLM-316L 耐蚀性降低的主要原因有:1)在较高的扫描速度下,SLM-316L 的位错密度增大,材料内部元素分布的非均匀性增大,Mn<sub>7</sub>C<sub>3</sub> 纳米颗粒的尺寸增

大,导致奥氏体基体局部位置贫 Cr,促使点蚀坑形成<sup>[129]</sup>;2)SLM-316L 材料熔池附近的缺陷、孔洞以及大量的非平衡相也是其耐蚀性下降的原因,孔洞的几何形状及连通性是影响材料耐蚀性的两个关键因素<sup>[130]</sup>,腐蚀优先发生在直径较大的缺陷位置处,而直径较小(约 10 μm)的孔洞位置仍然处于钝化状态。已有研究证实采用传统方式制备的不锈钢因存在 MnS

夹杂物而会形成点蚀坑的形核位点,从而导致材料的耐蚀性降低<sup>[131]</sup>。Chao 等<sup>[132]</sup>认为 SLM-316L 在凝固过程中的冷却速率极高(约  $10^7$  K/s),使得成形件内不含 MnS 夹杂物,亦即不存在贫 Cr 区,能够有效抑制点蚀形核位点的形成。Sander 等<sup>[131]</sup>的研究也表明,由于熔池的快速凝固,MnS 夹杂物要么无法从中转化而湮灭,要么因尺寸太过细小而无法触发点蚀的形成,因此 SLM-316L 材料的耐蚀性优于锻件。值得一提的是,Sun 等<sup>[82]</sup>制备的 SLM-316L 晶体层片状结构[如图 8(h)所示]具有极高的耐蚀性,材料的击穿电位高达 1.2 V,接近氧化铬热力学稳定的极限电位。

#### 4.4 退火态 SLM-316L 的拉伸性能

在成形过程中,SLM-316L 材料经历了复杂的热历史,导致打印态样件中通常存在较大的残余应力,因此利用热处理手段使微结构均匀化、消除残余应力是

当前进一步提升打印态构件力学性能不可或缺的步骤<sup>[90,133]</sup>。笔者研究了 SLM-316L 材料微观组织(熔池、晶粒及胞结构,如图 14 所示)与拉伸性能随退火温度的演化规律<sup>[83]</sup>,结果表明:当热处理温度较低( $\leq 873$  K)时,材料的屈服强度与打印态材料相近。这是因为当退火温度较低时,相当于去应力退火<sup>[130]</sup>,尽管晶粒尺寸可能会出现明显变化<sup>[18,83]</sup>,但是胞结构是稳定存在的,并且其尺寸几乎保持不变(如图 14 所示),因而材料的屈服强度与打印态材料几乎相同。文献<sup>[83,90-91]</sup>也得到了相似的规律。值得注意的是,由于低温退火会促进材料内部非平衡微观结构和微观应力发生松弛,因此材料的加工硬化行为有所改变<sup>[83,90,133]</sup>。进一步提高退火温度,SLM-316L 的非均匀层级结构逐渐消失<sup>[83,90,134]</sup>,材料的屈服强度降低,延伸率提高,表现出经典的“Trade-off”行为。图 15 总

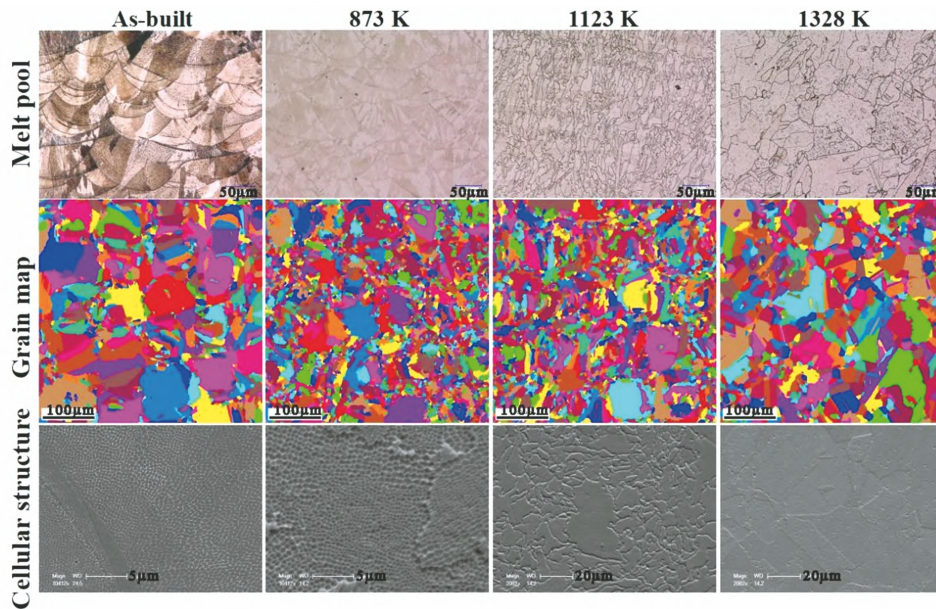


图 14 SLM-316L 熔池、晶粒及胞结构随退火温度的演化<sup>[83]</sup>

Fig. 14 Melt pool, crystalline grain, and cellular structure of selective laser melted 316L stainless steel evolution as a function of annealing temperature<sup>[83]</sup>

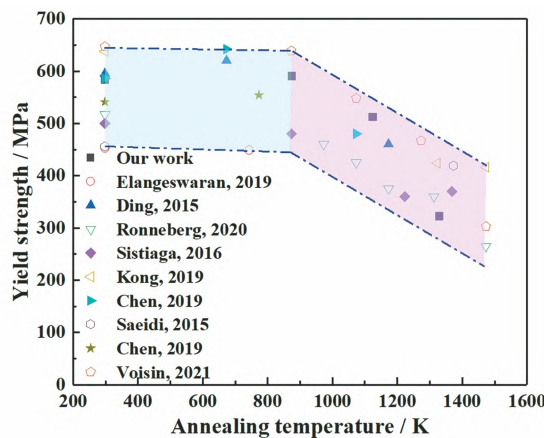


图 15 SLM-316L 屈服强度随退火温度的变化<sup>[83]</sup>,图中数据来自文献<sup>[18,84-85,87,90,92,117,123,133]</sup>,蓝色虚线为屈服强度随退火温度的总体变化趋势

Fig. 15 Variation of yield strength of selective laser melted 316L with annealing temperature<sup>[83]</sup>, and the data in the figure are from the literatures<sup>[18,84-85,87,90,92,117,123,133]</sup>, where the blue dashed lines indicate the general variation trend

总结了不同文献中报道的拉伸性能数据。虽然打印态 SLM-316L 的屈服强度数值较为分散 (450 ~ 650 MPa),但其随退火温度的变化趋势是一致的,即: 873 K 退火后, SLM-316L 的屈服强度几乎不变,这与观察到的胞状结构的稳定性是一致的(图 14);继续提高退火温度,熔池、胞结构等逐渐消失,材料的屈服强度降低。值得注意的是,热处理可以显著提高打印态 SLM-316L 的应变硬化能力。笔者研究发现,当热处理温度提高到固溶温度时(约 1000 °C),材料的加工硬化能力几乎是打印态材料的 3 倍<sup>[83]</sup>,这主要是由材料内部的层级非均匀微结构消失以及 SLM-316L 材料的位错密度大幅降低导致。

## 5 SLM-316L 不锈钢的应用

图 16 总结了 SLM-316L 不锈钢的几种典型应用;在生物医学方面,针对病人的需求,通过 CAD 建

模实现了 SLM-316L 下颌正畸托架、牙冠及牙桥等多种牙科产品的定制,如图 16(a)所示<sup>[135-136]</sup>;在核能工业方面,316L 不锈钢常被用于制造国际热核实验反应堆中的真空容器以及带有复杂内部管道的系统<sup>[19,130]</sup>,如,He 等<sup>[137]</sup>利用 SLM-316L 制备了用于小型核反应堆的燃料储存支架,并讨论了 SLM 技术全面应用于核能工业面临的技术问题,如图 16(b)所示;在轻量化结构设计方面,点阵结构在承载、吸能、隔热、减震等领域具有广阔的应用前景,主要应用于承受载荷不大但具备多功能效果的非关键承载构件,可以应用在航空航天、海洋、交通等领域,图 16(c)显示了 SLM-316L 制备多种复杂点阵结构的潜力<sup>[138-139]</sup>;在航空航天方面,SLM 制造的 316L 零件可同时满足航空航天领域对产品高强度、轻量化的要求,能用于制造液体火箭发动机喷油器<sup>[140]</sup>,如图 16(d)所示。

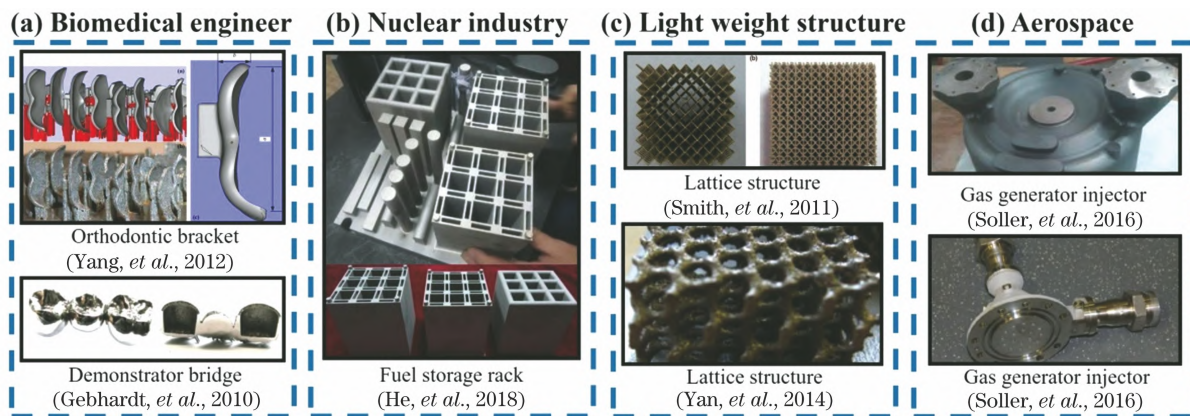


图 16 SLM-316L 的应用<sup>[135-140]</sup>

Fig. 16 Applications of selective laser melted 316L stainless steel<sup>[135-140]</sup>

## 6 结束语

本文综述了 SLM-316L 跨尺度非均匀层级结构中熔池、晶粒、胞结构及纳米氧化物颗粒等的研究现状,比较了几种常用的度量指标以及几个无量纲数对致密度的影响规律,总结了熔池形貌的无量纲表达式的研究现状,分析了熔池形貌与晶体学织构之间的关系,重点讨论了 SLM-316L 不锈钢中胞结构的形成机理以及预测 SLM-316L 不锈钢屈服强度存在的争议性问题。此外,本文对 SLM-316L 的耐蚀性及其随退火温度的变化规律也进行了简要总结。随着研究的不断深入以及该技术的快速发展,SLM-316L 的研究也存在一些亟待解决的问题与挑战,笔者认为以下方向值得进一步关注:

1)打印态 SLM-316L 形成了跨越 6 个数量级的非均匀层级结构。在复杂的热循环作用下,材料的微观结构呈现从“介观”到“微观”的组织特征,而且纳米颗粒、元素再分布及位错密度等不仅与成形工艺参数有关,还具有一定的空间相关性,从而导致准确量化某一

工艺下的微结构较为困难,目前只能通过横向对比的方法,采用多种形式的表征手段分析材料的微观结构和相应的化学非均匀性。通过调整工艺参数来控制胞结构尺寸、织构和位错密度是当前提升 SLM-316L 综合力学性能的关键,其中 SLM-316L 胞结构的形成机理及打印态材料屈服强度所服从的预测规律还值得进行更深入的研究。

2)量化缺陷对 SLM-316L 材料拉伸性能及耐蚀性的影响。SLM-316L 成形件难免存在欠熔、孔洞及裂纹等缺陷,这些缺陷的存在会降低材料的力学性能。然而,SLM 是一种面向材料的“域控制”制造技术,仅用致密度这一指标无法刻画缺陷的特征长度、形状及分布等对 SLM-316L 材料力学性能的影响。更重要的是,SLM-316L 拉伸测试及耐蚀性测试缺乏相应的标准。因此,发展考虑缺陷特征参量的理论模型并建立相关的测试标准,不仅有助于缩短研发周期,揭示该技术背后的基础科学问题,还有利于 SLM-316L 材料的大规模推广及应用。

3)目前,大部分已发表的研究成果是基于简单块

体试样取得的,而实际生产的复杂构件,其打印位置及横截面积是变化的,在横截面积较小位置处的缺陷对材料力学性能的影响更为突出,仅使用拉伸试样较难全面反映某一打印工艺下构件的力学性能水平。而且,大量研究工作所报道的拉伸性能测试结果是基于非标试样取得的,有待系统考察拉伸试样在具有不同横截面形状及尺寸下的力学性能响应,厘清拉伸试样的几何形状及尺寸对 SLM-316L 力学性能(尤其是断后延伸率)的影响,得到评价 SLM 材料拉伸性能的最佳试样几何尺寸,从而推动 SLM 材料拉伸测试标准的建立。

### 参 考 文 献

- [1] Yan C Z, Hao L, Hussein A, et al. Ti-6Al-4V triply periodic minimal surface structures for bone implants fabricated via selective laser melting[J]. *Journal of the Mechanical Behavior of Biomedical Materials*, 2015, 51: 61-73.
- [2] 王华明,张述泉,王韬,等. 激光增材制造高性能大型钛合金构件凝固晶粒形态及显微组织控制研究进展[J]. *西华大学学报(自然科学版)*, 2018, 37(4): 9-14.  
Wang H M, Zhang S Q, Wang T, et al. Progress on solidification grain morphology and microstructure control of laser additively manufactured large titanium components [J]. *Journal of Xihua University (Natural Science Edition)*, 2018, 37(4): 9-14.
- [3] Kalinin G, Barabash V, Cardella A, et al. Assessment and selection of materials for ITER in-vessel components [J]. *Journal of Nuclear Materials*, 2000, 283/284/285/286/287: 10-19.
- [4] DebRoy T, Wei H L, Zuback J S, et al. Additive manufacturing of metallic components-process, structure and properties [J]. *Progress in Materials Science*, 2018, 92: 112-224.
- [5] ASTM Committee. Standard terminology for additive manufacturing technologies: F2792-12a [S]. West Conshohocken: ASTM International, 2012.
- [6] Bajaj P, Hariharan A, Kini A, et al. Steels in additive manufacturing: a review of their microstructure and properties [J]. *Materials Science and Engineering A*, 2020, 772: 138633.
- [7] Yin Y, Tan Q Y, Bermingham M, et al. Laser additive manufacturing of steels [J]. *International Materials Reviews*, 2021: 1-87.
- [8] Fayazfar H, Salarian M, Rogalsky A, et al. A critical review of powder-based additive manufacturing of ferrous alloys: process parameters, microstructure and mechanical properties [J]. *Materials & Design*, 2018, 144: 98-128.
- [9] Gorsse S, Hutchinson C, Gouné M, et al. Additive manufacturing of metals: a brief review of the characteristic microstructures and properties of steels, Ti-6Al-4V and high-entropy alloys [J]. *Science and Technology of Advanced Materials*, 2017, 18(1): 584-610.
- [10] 顾冬冬,张红梅,陈洪宇,等. 航空航天高性能金属材料构件激光增材制造[J]. *中国激光*, 2020, 47(5): 0500002.  
Gu D D, Zhang H M, Chen H Y, et al. Laser additive manufacturing of high-performance metallic aerospace components [J]. *Chinese Journal of Lasers*, 2020, 47(5): 0500002.
- [11] 王华明,张述泉,王向明. 大型钛合金结构件激光直接制造的进展与挑战(邀请论文) [J]. *中国激光*, 2009, 36(12): 3204-3209.  
Wang H M, Zhang S Q, Wang X M. Progress and challenges of laser direct manufacturing of large titanium structural components(invited paper) [J]. *Chinese Journal of Lasers*, 2009, 36(12): 3204-3209.
- [12] Sing S L, Yeong W Y. Laser powder bed fusion for metal additive manufacturing: perspectives on recent developments [J]. *Virtual and Physical Prototyping*, 2020, 15(3): 359-370.
- [13] 林鑫,杨海欧,陈静,等. 激光快速成形过程中 316L 不锈钢显微组织的演变[J]. *金属学报*, 2006, 42(4): 361-368.  
Lin X, Yang H O, Chen J, et al. Microstructure evolution of 316L stainless steel during laser rapid forming [J]. *Acta Metallurgica Sinica*, 2006, 42(4): 361-368.
- [14] Sun Z, Tan X, Tor S B, et al. Simultaneously enhanced strength and ductility for 3D-printed stainless steel 316L by selective laser melting [J]. *NPG Asia Materials*, 2018, 10(4): 127-136.
- [15] Saeidi K, Gao X, Zhong Y, et al. Hardened austenite steel with columnar sub-grain structure formed by laser melting [J]. *Materials Science and Engineering A*, 2015, 625: 221-229.
- [16] Tucho W M, Lysne V H, Austbø H, et al. Investigation of effects of process parameters on microstructure and hardness of SLM manufactured SS316L [J]. *Journal of Alloys and Compounds*, 2018, 740: 910-925.
- [17] Zhang B, Li Y T, Bai Q. Defect formation mechanisms in selective laser melting: a review [J]. *Chinese Journal of Mechanical Engineering*, 2017, 30(3): 515-527.
- [18] 丁利,李怀学,王玉岱,等. 热处理对激光选区熔化成形 316 不锈钢组织与拉伸性能的影响 [J]. *中国激光*, 2015, 42(4): 0406003.  
Ding L, Li H X, Wang Y D, et al. Heat treatment on microstructure and tensile strength of 316 stainless steel by selective laser melting [J]. *Chinese Journal of Lasers*, 2015, 42(4): 0406003.
- [19] Zhong Y, Liu L F, Wikman S, et al. Intragranular cellular segregation network structure strengthening 316L stainless steel prepared by selective laser melting [J]. *Journal of Nuclear Materials*, 2016, 470: 170-178.
- [20] Smith W L, Roehling J D, Strantza M, et al. Residual stress analysis of *in situ* surface layer heating effects on laser powder bed fusion of 316L stainless steel [J]. *Additive Manufacturing*, 2021, 47: 102252.
- [21] Saeidi K, Kvetková L, Lofaj F, et al. Austenitic stainless steel strengthened by the *in situ* formation of oxide nanoinclusions [J]. *RSC Advances*, 2015, 5(27): 20747-20750.
- [22] Yadroitsev I. Selective laser melting: direct manufacturing of 3D-objects by selective laser melting of metal powders [M]. Chisinau: LAP Lambert Academic Publishing, 2009.
- [23] Qiu C, Kindi M A, Aladawi A S, et al. A comprehensive study on microstructure and tensile behaviour of a selectively laser melted stainless steel [J]. *Scientific Reports*, 2018, 8: 7785.
- [24] Wang Y M, Voisin T, McKeown J T, et al. Additively manufactured hierarchical stainless steels with high strength and ductility [J]. *Nature Materials*, 2018, 17(1): 63-71.
- [25] Ma M M, Wang Z M, Zeng X Y. A comparison on metallurgical behaviors of 316L stainless steel by selective laser melting and laser cladding deposition [J]. *Materials Science and Engineering A*, 2017, 685: 265-273.
- [26] Jiang H Z, Li Z Y, Feng T, et al. Effect of process parameters on defects, melt pool shape, microstructure, and tensile behavior of 316L stainless steel produced by selective laser melting [J]. *Acta Metallurgica Sinica (English Letters)*, 2021, 34(4): 495-510.
- [27] Saboori A, Aversa A, Marchese G, et al. Microstructure and mechanical properties of AISI 316L produced by directed energy deposition-based additive manufacturing: a review [J]. *Applied Sciences*, 2020, 10(9): 3310.
- [28] Jiang H Z, Li Z Y, Feng T, et al. Factor analysis of selective laser melting process parameters with normalised quantities and Taguchi method [J]. *Optics & Laser Technology*, 2019, 119: 105592.
- [29] Sames W J, Medina F, Peter W H, et al. Effect of process control and powder quality on Inconel 718 produced using



- electron beam melting [M]. Hoboken: John Wiley & Sons, Inc., 2014: 409-423.
- [30] Mukherjee T, Zuback J S, De A, et al. Printability of alloys for additive manufacturing[J]. *Scientific Reports*, 2016, 6: 19717.
- [31] Juechter V, Scharowsky T, Singer R F, et al. Processing window and evaporation phenomena for Ti-6Al-4V produced by selective electron beam melting[J]. *Acta Materialia*, 2014, 76: 252-258.
- [32] Letenneur M, Brailovski V, Kreitsberg A, et al. Laser powder bed fusion of water-atomized iron-based powders: process optimization [J]. *Journal of Manufacturing and Materials Processing*, 2017, 1(2): 23.
- [33] Larimian T, Kannan M, Grzesiak D, et al. Effect of energy density and scanning strategy on densification, microstructure and mechanical properties of 316L stainless steel processed via selective laser melting[J]. *Materials Science and Engineering A*, 2020, 770: 138455.
- [34] Wang D, Song C H, Yang Y Q, et al. Investigation of crystal growth mechanism during selective laser melting and mechanical property characterization of 316L stainless steel parts [J]. *Materials & Design*, 2016, 100: 291-299.
- [35] Montero-Sistiaga M L, Godino-Martinez M, Boschmans K, et al. Microstructure evolution of 316L produced by HP-SLM (high power selective laser melting) [J]. *Additive Manufacturing*, 2018, 23: 402-410.
- [36] Gu D D, Shen Y F. Effects of processing parameters on consolidation and microstructure of W-Cu components by DMLS [J]. *Journal of Alloys and Compounds*, 2009, 473(1/2): 107-115.
- [37] Yadroitsev I, Bertrand P, Smurov I. Parametric analysis of the selective laser melting process [J]. *Applied Surface Science*, 2007, 253(19): 8064-8069.
- [38] Gu D D, Shen Y F. Balling phenomena in direct laser sintering of stainless steel powder: metallurgical mechanisms and control methods[J]. *Materials & Design*, 2009, 30(8): 2903-2910.
- [39] Kruth J P, Froyen L, van Vaerenbergh J, et al. Selective laser melting of iron-based powder [J]. *Journal of Materials Processing Technology*, 2004, 149(1/2/3): 616-622.
- [40] Song Y A, Koenig W. Experimental study of the basic process mechanism for direct selective laser sintering of low-melting metallic powder[J]. *CIRP Annals*, 1997, 46(1): 127-130.
- [41] Niu H J, Chang I T H. Selective laser sintering of gas atomized M2 high speed steel powder[J]. *Journal of Materials Science*, 2000, 35(1): 31-38.
- [42] Carter L N, Wang X, Read N, et al. Process optimisation of selective laser melting using energy density model for nickel based superalloys[J]. *Materials Science and Technology*, 2016, 32(7): 657-661.
- [43] Casalino G, Campanelli S L, Contuzzi N, et al. Experimental investigation and statistical optimisation of the selective laser melting process of a maraging steel [J]. *Optics & Laser Technology*, 2015, 65: 151-158.
- [44] Thijs L, Verhaeghe F, Craeghs T, et al. A study of the microstructural evolution during selective laser melting of Ti-6Al-4V[J]. *Acta Materialia*, 2010, 58(9): 3303-3312.
- [45] Cherry J A, Davies H M, Mehmood S, et al. Investigation into the effect of process parameters on microstructural and physical properties of 316L stainless steel parts by selective laser melting [J]. *The International Journal of Advanced Manufacturing Technology*, 2015, 76(5/6/7/8): 869-879.
- [46] Gu D D, Shen Y F, Yang J L, et al. Effects of processing parameters on direct laser sintering of multicomponent Cu based metal powder[J]. *Materials Science and Technology*, 2006, 22(12): 1449-1455.
- [47] Thomas M, Baxter G J, Todd I. Normalised model-based processing diagrams for additive layer manufacture of engineering alloys[J]. *Acta Materialia*, 2016, 108: 26-35.
- [48] Kamath C, El-dasher B, Gallegos G F, et al. Density of additively-manufactured, 316L SS parts using laser powder-bed fusion at powers up to 400 W[J]. *The International Journal of Advanced Manufacturing Technology*, 2014, 74(1/2/3/4): 65-78.
- [49] Simchi A. Direct laser sintering of metal powders: mechanism, kinetics and microstructural features[J]. *Materials Science and Engineering A*, 2006, 428(1/2): 148-158.
- [50] Simchi A, Pohl H. Effects of laser sintering processing parameters on the microstructure and densification of iron powder[J]. *Materials Science and Engineering A*, 2003, 359(1/2): 119-128.
- [51] Song B, Dong S J, Deng S H, et al. Microstructure and tensile properties of iron parts fabricated by selective laser melting[J]. *Optics & Laser Technology*, 2014, 56: 451-460.
- [52] Laakso P, Riipinen T, Laukkanen A, et al. Optimization and simulation of SLM process for high density H13 tool steel parts [J]. *Physics Procedia*, 2016, 83: 26-35.
- [53] Mazur M, Leary M, McMillan M, et al. SLM additive manufacture of H13 tool steel with conformal cooling and structural lattices[J]. *Rapid Prototyping Journal*, 2016, 22(3): 504-518.
- [54] Dilip J J S, Ram G D J, Starr T L, et al. Selective laser melting of HY100 steel: process parameters, microstructure and mechanical properties[J]. *Additive Manufacturing*, 2017, 13: 49-60.
- [55] Kumar P, Farah J, Akram J, et al. Influence of laser processing parameters on porosity in Inconel 718 during additive manufacturing [J]. *The International Journal of Advanced Manufacturing Technology*, 2019, 103(1/2/3/4): 1497-1507.
- [56] Kasperovich G, Haubrich J, Gussone J, et al. Correlation between porosity and processing parameters in TiAl6V4 produced by selective laser melting [J]. *Materials & Design*, 2016, 105: 160-170.
- [57] Leicht A, Rashidi M, Klement U, et al. Effect of process parameters on the microstructure, tensile strength and productivity of 316L parts produced by laser powder bed fusion [J]. *Materials Characterization*, 2020, 159: 110016.
- [58] Wang Z K, Liu M B. Dimensionless analysis on selective laser melting to predict porosity and track morphology[J]. *Journal of Materials Processing Technology*, 2019, 273: 116238.
- [59] Gan Z, Kafka O L, Parab N, et al. Universal scaling laws of keyhole stability and porosity in 3D printing of metals [J]. *Nature Communications*, 2021, 12: 2379.
- [60] Montani M, Demir A G, Mostaed E, et al. Processability of pure Zn and pure Fe by SLM for biodegradable metallic implant manufacturing[J]. *Rapid Prototyping Journal*, 2017, 23(3): 514-523.
- [61] Wang Y M, Kamath C, Voisin T, et al. A processing diagram for high-density Ti-6Al-4V by selective laser melting[J]. *Rapid Prototyping Journal*, 2018, 24(9): 1469-1478.
- [62] Cunningham R, Narra S P, Montgomery C, et al. Synchrotron-based X-ray microtomography characterization of the effect of processing variables on porosity formation in laser power-bed additive manufacturing of Ti-6Al-4V[J]. *JOM*, 2017, 69(3): 479-484.
- [63] Fang T H, Li W L, Tao N R, et al. Revealing extraordinary intrinsic tensile plasticity in gradient nano-grained copper [J]. *Science*, 2011, 331(6024): 1587-1590.
- [64] Wu X L, Yang M X, Yuan F P, et al. Heterogeneous lamella structure unites ultrafine-grain strength with coarse-grain ductility[J]. *Proceedings of the National Academy of Sciences of the United States of America*, 2015, 112(47): 14501-14505.
- [65] Wei Y, Li Y, Zhu L, et al. Evading the strength-ductility trade-off dilemma in steel through gradient hierarchical nanotwins[J]. *Nature Communications*, 2014, 5: 3580.
- [66] 马明明. 两种典型金属零部件激光增材制造技术基础比较研究 [D]. 武汉: 华中科技大学, 2016.
- Ma M M. A comparative study on fundamentals of two typical

- laser additive manufacturing technologies of metallic components [D]. Wuhan: Huazhong University of Science and Technology, 2016.
- [67] Ma M M, Wang Z M, Gao M, et al. Layer thickness dependence of performance in high-power selective laser melting of 1Cr18Ni9Ti stainless steel [J]. *Journal of Materials Processing Technology*, 2015, 215: 142-150.
- [68] Yadroitsev I, Yadroitsava I, Bertrand P, et al. Factor analysis of selective laser melting process parameters and geometrical characteristics of synthesized single tracks [J]. *Rapid Prototyping Journal*, 2012, 18(3): 201-208.
- [69] Casati R, Lemke J, Vedani M. Microstructure and fracture behavior of 316L austenitic stainless steel produced by selective laser melting [J]. *Journal of Materials Science & Technology*, 2016, 32(8): 738-744.
- [70] Zhao C, Fezzaa K, Cunningham R W, et al. Real-time monitoring of laser powder bed fusion process using high-speed X-ray imaging and diffraction [J]. *Scientific Reports*, 2017, 7: 3602.
- [71] Leung C L A, Marussi S, Atwood R C, et al. *In situ* X-ray imaging of defect and molten pool dynamics in laser additive manufacturing [J]. *Nature Communications*, 2018, 9: 1355.
- [72] Cunningham R, Zhao C, Parab N, et al. Keyhole threshold and morphology in laser melting revealed by ultrahigh-speed X-ray imaging [J]. *Science*, 2019, 363(6429): 849-852.
- [73] Kurzynowski T, Gruber K, Stopyra W, et al. Correlation between process parameters, microstructure and properties of 316L stainless steel processed by selective laser melting [J]. *Materials Science and Engineering A*, 2018, 718: 64-73.
- [74] Bertoli U S, Wolfer A J, Matthews M J, et al. On the limitations of volumetric energy density as a design parameter for selective laser melting [J]. *Materials & Design*, 2017, 113: 331-340.
- [75] Yan W T, Ge W J, Qian Y, et al. Multi-physics modeling of single/multiple-track defect mechanisms in electron beam selective melting [J]. *Acta Materialia*, 2017, 134: 324-333.
- [76] Yan W T, Lian Y P, Yu C, et al. An integrated process-structure-property modeling framework for additive manufacturing [J]. *Computer Methods in Applied Mechanics and Engineering*, 2018, 339: 184-204.
- [77] Ion J C, Shercliff H R, Ashby M F. Diagrams for laser materials processing [J]. *Acta Metallurgica et Materialia*, 1992, 40(7): 1539-1551.
- [78] Niendorf T, Leuders S, Riemer A, et al. Highly anisotropic steel processed by selective laser melting [J]. *Metallurgical and Materials Transactions B*, 2013, 44(4): 794-796.
- [79] Fergani O, Brotan V, Bambach M, et al. Texture evolution in stainless steel processed by selective laser melting and annealing [J]. *Materials Science and Technology*, 2018, 34(18): 2223-2230.
- [80] Marattukalam J J, Karlsson D, Pacheco V, et al. The effect of laser scanning strategies on texture, mechanical properties, and site-specific grain orientation in selective laser melted 316L SS [J]. *Materials & Design*, 2020, 193: 108852.
- [81] Andreau O, Koutiri I, Peyre P, et al. Texture control of 316L parts by modulation of the melt pool morphology in selective laser melting [J]. *Journal of Materials Processing Technology*, 2019, 264: 21-31.
- [82] Sun S H, Ishimoto T, Hagihara K, et al. Excellent mechanical and corrosion properties of austenitic stainless steel with a unique crystallographic lamellar microstructure via selective laser melting [J]. *Scripta Materialia*, 2019, 159: 89-93.
- [83] Jiang H Z, Li Z Y, Feng T, et al. Effect of annealing temperature and strain rate on mechanical property of a selective laser melted 316L stainless steel [J]. *Acta Metallurgica Sinica (English Letters)*, 2021: 1-17.
- [84] Chen N, Ma G Q, Zhu W Q, et al. Enhancement of an additive-manufactured austenitic stainless steel by post-manufacture heat-treatment [J]. *Materials Science and Engineering A*, 2019, 759: 65-69.
- [85] Kong D C, Dong C F, Ni X Q, et al. Mechanical properties and corrosion behavior of selective laser melted 316L stainless steel after different heat treatment processes [J]. *Journal of Materials Science & Technology*, 2019, 35(7): 1499-1507.
- [86] Güden M, Yava H, Tanrıkulu A A, et al. Orientation dependent tensile properties of a selective-laser-melt 316L stainless steel [J]. *Materials Science and Engineering A*, 2021, 824: 141808.
- [87] Ronneberg T, Davies C M, Hooper P A. Revealing relationships between porosity, microstructure and mechanical properties of laser powder bed fusion 316L stainless steel through heat treatment [J]. *Materials & Design*, 2020, 189: 108481.
- [88] Liu L F, Ding Q Q, Zhong Y, et al. Dislocation network in additive manufactured steel breaks strength-ductility trade-off [J]. *Materials Today*, 2018, 21(4): 354-361.
- [89] Shamsujjoha M, Agnew S R, Fitz-Gerald J M, et al. High strength and ductility of additively manufactured 316L stainless steel explained [J]. *Metallurgical and Materials Transactions A*, 2018, 49(7): 3011-3027.
- [90] Voisin T, Forien J B, Perron A, et al. New insights on cellular structures strengthening mechanisms and thermal stability of an austenitic stainless steel fabricated by laser powder-bed-fusion [J]. *Acta Materialia*, 2021, 203: 116476.
- [91] Salman O O, Gammer C, Chaubey A K, et al. Effect of heat treatment on microstructure and mechanical properties of 316L steel synthesized by selective laser melting [J]. *Materials Science and Engineering A*, 2019, 748: 205-212.
- [92] Sistiaga M M, Nardone S, Hautfenne C, et al. Effect of heat treatment of 316L stainless steel produced by selective laser melting (SLM) [C] // Proceedings of the 27th Annual International Solid Freeform Fabrication Symposium - An Additive Manufacturing Conference, August 8-10, 2016, the University of Texas at Austin, Austin, Texas, USA. Austin: Verlag Nicht Ermitteltbar, Solid Freeform Fabrication, 2016: 558-565.
- [93] Khodabakhshi F, Farshidianfar M H, Gerlich A P, et al. Microstructure, strain-rate sensitivity, work hardening, and fracture behavior of laser additive manufactured austenitic and martensitic stainless steel structures [J]. *Materials Science and Engineering A*, 2019, 756: 545-561.
- [94] Kou S. *Welding metallurgy* [M]. New Jersey: John Wiley & Sons, Inc., 2003, 431(446): 223-225.
- [95] McKeown J T, Kulovits A K, Liu C, et al. *In situ* transmission electron microscopy of crystal growth-mode transitions during rapid solidification of a hypoeutectic Al-Cu alloy [J]. *Acta Materialia*, 2014, 65: 56-68.
- [96] Prashanth K G, Eckert J. Formation of metastable cellular microstructures in selective laser melted alloys [J]. *Journal of Alloys and Compounds*, 2017, 707: 27-34.
- [97] Asta M, Beckermann C, Karma A, et al. Solidification microstructures and solid-state parallels: recent developments, future directions [J]. *Acta Materialia*, 2009, 57(4): 941-971.
- [98] Birnbaum A J, Steuben J C, Barrick E J, et al. Intrinsic strain aging,  $\Sigma 3$  boundaries, and origins of cellular substructure in additively manufactured 316L [J]. *Additive Manufacturing*, 2019, 29: 100784.
- [99] Holt D L. Dislocation cell formation in metals [J]. *Journal of Applied Physics*, 1970, 41(8): 3197-3201.
- [100] Mercelis P, Kruth J P. Residual stresses in selective laser sintering and selective laser melting [J]. *Rapid Prototyping Journal*, 2006, 12(5): 254-265.
- [101] Bertsch K M, de Bellefon G M, Kuehl B, et al. Origin of dislocation structures in an additively manufactured austenitic stainless steel 316L [J]. *Acta Materialia*, 2020, 199: 19-33.
- [102] Das S R, Riaz T, Shyamal S, et al. A quantitative assessment on the contribution of various dislocation substructures to flow stress in a fine-grain high-Mn steel [J]. *Materials Letters*,

- 2021, 300: 130216.
- [103] Ding Q Q, Bei H B, Yao X, et al. Temperature effects on deformation substructures and mechanisms of a Ni-based single crystal superalloy[J]. *Applied Materials Today*, 2021, 23: 101061.
- [104] Williamson G K, Hall W H. X-ray line broadening from filed aluminium and wolfram[J]. *Acta Metallurgica*, 1953, 1(1): 22-31.
- [105] Bahl S, Mishra S, Yazar K U, et al. Non-equilibrium microstructure, crystallographic texture and morphological texture synergistically result in unusual mechanical properties of 3D printed 316L stainless steel[J]. *Additive Manufacturing*, 2019, 28: 65-77.
- [106] Yin Y J, Sun J Q, Guo J, et al. Mechanism of high yield strength and yield ratio of 316L stainless steel by additive manufacturing[J]. *Materials Science and Engineering A*, 2019, 744: 773-777.
- [107] He B B, Hu B, Yen H W, et al. High dislocation density-induced large ductility in deformed and partitioned steels[J]. *Science*, 2017, 357(6355): 1029-1032.
- [108] Pham M S, Solenthaler C, Janssens K G F, et al. Dislocation structure evolution and its effects on cyclic deformation response of AISI 316L stainless steel[J]. *Materials Science and Engineering A*, 2011, 528(7/8): 3261-3269.
- [109] Taylor G I. The mechanism of plastic deformation of crystals. Part I: theoretical[J]. *Proceedings of the Royal Society of London Series A, Containing Papers of a Mathematical and Physical Character*, 1934, 145(855): 362-387.
- [110] ASM International Handbook Committee. Properties and selection: irons, steels, and high-performance alloys[M]. Almere: ASM International, 1990.
- [111] Lou X Y, Andresen P L, Rebak R B. Oxide inclusions in laser additive manufactured stainless steel and their effects on impact toughness and stress corrosion cracking behavior[J]. *Journal of Nuclear Materials*, 2018, 499: 182-190.
- [112] Zhang X, Cao H B, Yang X Y, et al. Enhanced thermal stability of the cellular structure through nano-scale oxide precipitation in 3D printed 316L stainless steel[J]. *Fusion Engineering and Design*, 2021, 164: 112213.
- [113] Kong D C, Dong C F, Wei S L, et al. About metastable cellular structure in additively manufactured austenitic stainless steels[J]. *Additive Manufacturing*, 2021, 38: 101804.
- [114] Cui L Q, Jiang S, Xu J H, et al. Revealing relationships between microstructure and hardening nature of additively manufactured 316L stainless steel[J]. *Materials & Design*, 2021, 198: 109385.
- [115] Krakhmalev P, Fredriksson G, Svensson K, et al. Microstructure, solidification texture, and thermal stability of 316 L stainless steel manufactured by laser powder bed fusion[J]. *Metals*, 2018, 8(8): 643.
- [116] Kamariah M N, Harun W W, Khalil N Z, et al. Effect of heat treatment on mechanical properties and microstructure of selective laser melting 316L stainless steel[J]. *IOP Conference Series: Materials Science and Engineering*, 2017, 257(1): 012021.
- [117] Saeidi K, Gao X, Lofaj F, et al. Transformation of austenite to duplex austenite-ferrite assembly in annealed stainless steel 316L consolidated by laser melting[J]. *Journal of Alloys and Compounds*, 2015, 633: 463-469.
- [118] Sun Z J, Tan X P, Tor S B, et al. Selective laser melting of stainless steel 316L with low porosity and high build rates[J]. *Materials & Design*, 2016, 104: 197-204.
- [119] Cramer S D, Covino B S. Corrosion: fundamentals, testing, and protection[M]. Almere: ASM International, 2003.
- [120] Lu K, Lu L, Suresh S. Strengthening materials by engineering coherent internal boundaries at the nanoscale[J]. *Science*, 2009, 324(5925): 349-352.
- [121] Lu K, Yan F K, Wang H T, et al. Strengthening austenitic steels by using nanotwinned austenitic grains[J]. *Scripta Materialia*, 2012, 66(11): 878-883.
- [122] Roach A M, White B C, Garland A, et al. Size-dependent stochastic tensile properties in additively manufactured 316L stainless steel[J]. *Additive Manufacturing*, 2020, 32: 101090.
- [123] Elangeswaran C, Cutolo A, Muralidharan G K, et al. Effect of post-treatments on the fatigue behaviour of 316L stainless steel manufactured by laser powder bed fusion[J]. *International Journal of Fatigue*, 2019, 123: 31-39.
- [124] Riemer A, Leuders S, Thöne M, et al. On the fatigue crack growth behavior in 316L stainless steel manufactured by selective laser melting[J]. *Engineering Fracture Mechanics*, 2014, 120: 15-25.
- [125] Suryawanshi J, Prashanth K G, Ramamurty U. Mechanical behavior of selective laser melted 316L stainless steel[J]. *Materials Science and Engineering A*, 2017, 696: 113-121.
- [126] Segura I A, Murr L E, Terrazas C A, et al. Grain boundary and microstructure engineering of Inconel 690 cladding on stainless-steel 316L using electron-beam powder bed fusion additive manufacturing[J]. *Journal of Materials Science & Technology*, 2019, 35(2): 351-367.
- [127] Yang M X, Yan D S, Yuan F P, et al. Dynamically reinforced heterogeneous grain structure prolongs ductility in a medium-entropy alloy with gigapascal yield strength[J]. *Proceedings of the National Academy of Sciences of the United States of America*, 2018, 115(28): 7224-7229.
- [128] Kazemipour M, Mohammadi M, Mfoumou E, et al. Microstructure and corrosion characteristics of selective laser-melted 316L stainless steel: the impact of process-induced porosities[J]. *JOM*, 2019, 71(9): 3230-3240.
- [129] Sprouster D J, Cunningham W S, Halada G P, et al. Dislocation microstructure and its influence on corrosion behavior in laser additively manufactured 316L stainless steel[J]. *Additive Manufacturing*, 2021, 47: 102263.
- [130] Kong D C, Ni X Q, Dong C F, et al. Heat treatment effect on the microstructure and corrosion behavior of 316L stainless steel fabricated by selective laser melting for proton exchange membrane fuel cells[J]. *Electrochimica Acta*, 2018, 276: 293-303.
- [131] Sander G, Thomas S, Cruz V, et al. On the corrosion and metastable pitting characteristics of 316L stainless steel produced by selective laser melting[J]. *Journal of the Electrochemical Society*, 2017, 164(6): C250-C257.
- [132] Chao Q, Cruz V, Thomas S, et al. On the enhanced corrosion resistance of a selective laser melted austenitic stainless steel[J]. *Scripta Materialia*, 2017, 141: 94-98.
- [133] Chen W, Voisin T, Zhang Y, et al. Microscale residual stresses in additively manufactured stainless steel[J]. *Nature Communications*, 2019, 10: 4338.
- [134] Li W, Li S, Liu J, et al. Effect of heat treatment on AlSi10Mg alloy fabricated by selective laser melting: microstructure evolution, mechanical properties and fracture mechanism[J]. *Materials Science and Engineering A*, 2016, 663: 116-125.
- [135] Yang Y Q, Lu J B, Luo Z Y, et al. Accuracy and density optimization in directly fabricating customized orthodontic production by selective laser melting[J]. *Rapid Prototyping Journal*, 2012, 18(6): 482-489.
- [136] Gebhardt A, Schmidt F M, Hötter J S, et al. Additive manufacturing by selective laser melting the realizer desktop machine and its application for the dental industry[J]. *Physics Procedia*, 2010, 5: 543-549.
- [137] He X M, Zhu Z Q, Shao C L, et al. Additive manufacturing of spent fuel storage rack model by selective laser melting[C]// ASME 2018 Nuclear Forum, June 24-28, 2018, Lake Buena Vista, Florida, USA. New York: American Society of Mechanical Engineers, 2018: V001T02A001.
- [138] Smith M, Cantwell W J, Guan Z, et al. The quasi-static and blast response of steel lattice structures[J]. *Journal of*

- [139] Yan C Z, Hao L, Hussein A, et al. Advanced lightweight 316L stainless steel cellular lattice structures fabricated via selective laser melting[J]. *Materials & Design*, 2014, 55: 533-541.
- [140] Soller S, Barata A, Beyer S, et al. Selective laser melting (SLM) of Inconel 718 and stainless steel injectors for liquid rocket engines[C]//*Space Propulsion 2016 Proceedings*, May 2-6, 2016, Rome, Italy. [S.l.: s.n.], 2016.

## State of the Art of Selective Laser Melted 316L Stainless Steel: Process, Microstructure, and Mechanical Properties

Jiang Huazhen<sup>1</sup>, Fang Jiahuiyu<sup>1,2</sup>, Chen Qisheng<sup>1,2\*</sup>, Yao Shaoke<sup>1,2</sup>, Sun Huilei<sup>3</sup>,  
Hou Jingyu<sup>1,2</sup>, Hu Qiyun<sup>1,2</sup>, Li Zhengyang<sup>1,2\*\*</sup>

<sup>1</sup> Wide Field Flight Engineering Science and Application Center, Institute of Mechanics, Chinese Academy of Science, Beijing 100190, China;

<sup>2</sup> School of Engineering Science, University of Chinese Academy of Sciences, Beijing 100049, China;

<sup>3</sup> School of Mechanical Engineering, Hebei University of Science & Technology, Shijiazhuang 050018, Hebei, China

### Abstract

**Significance** Metal additive manufacturing can be used to manufacture complex structural components that are difficult or even impossible to be produced using conventional methods. Recent development in constituent technologies has improved the understanding of process parameter-structure-property relationships for as-printed parts; 316L stainless steel (SS) is a face-centered cubic material, and the structure is not transformed when cooled to room temperature. Therefore, it is a good candidate material for analyzing the influence of heterogeneous microstructures on the mechanical performance of additive manufacturing (AM)-processed materials. Several studies have revealed that the strength and ductility of selective-laser-melted (SLM) 316L SS are higher than those of forged SS. This is because SLM parts have unique heterogeneous microstructures. Here, we review the recent SLM 316L SS, considering the process parameters, trans-scale structures, and mechanical properties. We provide a detailed review of SLM 316L SS with high strength and ductility and give insight into the future of this material.

**Progress** First, defect formation mechanisms in SLM 316L SS are discussed. To summarize and compare the process-parameter-dependent relative density of as-printed samples, different energy density indices are adopted to calculate the resultant energy density under different processing conditions (i. e., different selective laser melting machines, spot diameters, and materials). Then, the melt pool evolutions with different process parameters are reported. We summarize the relationship between the melt pool geometry and crystallographic texture and present the melt pool morphology predicted through dimensionless analysis. Thereafter, the grain size and morphology, cellular structure, dislocation density, and nanoparticles of SLM 316L samples are discussed, focusing on the formation mechanism of cellular structures, followed by the presentation of the mechanical performance, including hardness, tensile properties, and corrosion behavior, of SLM 316L parts. Additionally, the effects of postdeposition heat treatment on the microstructures and tensile properties are also reviewed.

With an increase in various energy density indices, the relative density of the part increases first, remains constant, and then decreases (Fig. 2). Several dimensionless quantities, including  $R_{HD}$ ,  $\eta_m$ ,  $\eta_v$ , and  $Ke_m L_d^*$ , are used to determine the minimum threshold for as-printed samples with high relative densities, and their values are 1.2, 2.6, 0.45, and 2.0, respectively (Fig. 3). The energy density imported into a powder bed has a significant impact on melt pool morphology (Figs. 5–8). However, contradictory results are observed when different energy density indices are used (Fig. 5), suggesting that there are limitations in using these indices as design parameters for selective laser melting. Comparing reported data for SLM and forged materials, it is observed that the grain size of SLM 316L SS is relatively large (Table 1). An anisotropic grain structure, namely, a checkerboard-like structure, is formed on the top surface, whereas a columnar grain structure is formed on the side plane of the as-built 316L SS, with the grain-size aspect ratio ranging from 1.4 to 15. Although the formation mechanism of the cellular structure is still not clarified, the structure plays a vital role in determining the mechanical performance of SLM parts. Nevertheless, as-printed materials have massive dislocation networks at the cell boundaries. Such cell structures with dislocations formed in SLM material are similar to the microstructure processed under severe plastic deformation processes. Many studies have reported that high dislocation densities, ranging from  $10^{14}$  to  $10^{15} \text{ m}^{-2}$ , are obtained in as-built 316L SS, which contributes significantly to the enhanced tensile yield strength of SLM samples according to the Taylor hardening law. Recently, it has been reported that SLM 316L samples break through the strength-ductility tradeoff due to their hierarchical microstructure

(Table 2 and Fig. 11). By tailoring laser process parameters, the melt pool shape, cell structure size, and size/content of nanoinclusions may change; hence, different strengthening mechanisms will be dominated at a certain printing process (Fig. 11). We infer that the hierarchically heterogeneous microstructure acts as a whole to resist tensile deformation under loading. Our experimental results collectively suggest that melt pool, grain, and cell structure boundaries are relatively weak regions in SLM parts, and the original grains of an SLM part are usually subdivided after tensile deformation (Figs. 12–13). Though the thermal stability of various microstructural features may differ (Fig. 14), independent of the process parameters and printing machines, 873 K is the temperature threshold above which SLM 316L SS exhibits classical strength-ductility tradeoff (Fig. 15).

**Conclusions and Prospects** In this study, we present a comprehensive overview of the evolution of the microstructures of SLM 316L SS from heterogeneous aspects. Unique microstructures, including the presence of crystalline grains, defects, melt pools, cellular structures, very high dislocation density similar to that of a severely plastically deformed material, and nanoinclusions, are formed in SLM 316L SS. Many studies have shown that the mechanical properties of SLM 316L SS are comparable with those of the wrought counterparts, though the mechanical performances may vary with process parameters and change locally within a part. Progress has been made in understanding SLM 316L SS, and the underlying strengthening mechanisms have been sufficiently revealed. Therefore, tailoring the structure and properties of SLM 316L based on scientific principles paves the way to AM metal parts with excellent mechanical properties. This review can serve as a valuable reference for understanding the current state of SLM 316L SS, the scientific gaps, and future research needed to advance this technology.

**Key words** laser technique; additive manufacturing; selective laser melting; 316L stainless steel; hierarchically heterogeneous microstructure; mechanical properties